*J. Fluid Mech.* (1993), *vol.* 257, *pp.* 373–401

# Investigation of the stable interaction of a passive compliant surface with a turbulent boundary layer

By **T. LEE, M. FISHER AND W. H. SCHWARZ**
Department of Chemical Engineering, The Johns Hopkins University, Baltimore,
MD 21218, USA

(Received 26 June 1992 and in revised form 7 May 1993)

The near-wall flow structure of a zero-pressure-gradient flat-plate turbulent boundary layer with a single-layer viscoelastic compliant surface was visualized using the hydrogen-bubble technique. The compliant materials were made by mixing silicone elastomer with silicone oil. The flow-visualization experiments indicated low-speed wall streaks with increased spanwise spacing and elongated spatial coherence compared to those obtained on a rigid surface. More interestingly, an intermittent relaminarization-like phenomenon was observed at low Reynolds numbers for the particular compliant surface investigated. Apparently, the observed changes in the near-wall flow structure over the compliant surface are caused by the stable interaction between the compliant surface and the turbulent flow-field. Optical holographic interferometry and laser Doppler velocimetry were also employed to obtain the basic parameters of the turbulent boundary layers and the flow-induced compliant-surface displacements to better understand the physics of the interaction between a turbulent boundary layer and a passive compliant surface.

## 1. Introduction

The motion of a turbulent flow over a compliant surface causes a variety of fluid/solid interactions which have been actively studied for three decades (Blick & Walters 1968; Hansen & Hunston 1974, 1983, Bushnell, Hefner & Ash 1977; McMichael, Klebanoff & Mease 1979; Hansen, Hunston & Ni 1980; Gad-el-Hak, Blackwelder & Riley 1984; Duncan, Waxman & Tulin 1985; Duncan 1986; Gad-el-Hak 1986*a*, *b*, 1987; Riley, Gad-el-Hak & Metcalf 1988; Hess 1990). The idea of using a compliant coating to alter a flow field was initially suggested by Kramer (1957) based on his observation of the swimming speeds of dolphins. It was thought that the pliability of dolphin skin caused the shear-layer fluctuations to be damped, thereby leading to an extended region of the laminar boundary layer (delayed transition), and affecting the turbulent boundary layer so as to produce significant drag reduction.

Recent linear stability analyses of the Blasius flow show that significant stabilization of the Tollmien–Schlichting instabilities can be achieved by use of an appropriate compliant coating (Carpenter & Garrad 1985, 1986; Yeo 1988; Carpenter 1990). An increase in the transition Reynolds number of 300% above that for a rigid wall has been predicted for a Blasius boundary layer over a single-layer isotropic viscoelastic compliant surface in the absence of the flow-induced compliant-surface instability (Yeo 1988). A substantial drag reduction was reported by Blick & Walters (1968) using a particular flexible surface beneath a turbulent boundary layer; however, McMichael *et al.* (1979) obtained an increase in the drag in a seemingly identical set of experiments designed to confirm the original finding. Irreproducibility seems to be an outstanding characteristic of compliant surface experiments.

Later experimental and theoretical work has not provided a definitive answer to the question of how surface compliance affects turbulent drag and noise generation. The interaction between a passive compliant surface and a turbulent boundary layer is still not well understood. Recent experimental investigations (McMichael *et al.* 1979; Hansen *et al.* 1980; Gad-el-Hak *et al.* 1984) indicate that a fluid/solid interaction caused by the surface compliance may result in hydroelastic instabilities, in the form of large-amplitude, static-divergence waves, which develop on viscoelastic compliant surfaces with the ratio of the free-stream velocity $U_0$ to the transverse-wave speed in solid $C_t$ ( $= (G/\rho_s)^{\frac{1}{2}}$, where $G$ and $\rho_s$ are the shear modulus of rigidity and density of the compliant material) exceeds a critical value $R_c$ ($R_c = U_s/C_t$, where $U_s$ is the onset velocity for the static-divergence waves to occur). The appearance of static-divergence wave depends on the material and flow parameters. Gad-el-Hak *et al.* (1984) also reported that the value of $U_s$ depends on the geometrical and mechanical properties of the coating (e.g. the thickness of the compliant material $d$, $G$, $\rho_s$ and $U_0$). $R_c$ decreases as $d$ increases and approaches a theoretical value of 3 for large $d$, according to Duncan *et al.* (1985). The presence of these large-amplitude compliant-surface deformations was always accompanied by an increase in the skin friction drag. Past investigations (Hansen & Hunston 1974; McMichael *et al.* 1979; Hansen *et al.* 1980; Gad-el-Hak *et al.* 1984; and others) suggest that in order to provide a net reduction of skin-friction drag, it is necessary that the amplitude of the surface motions be kept low enough to avoid causing a 'roughness' effect which would increase, rather than decrease, the drag.

For a rigid-surface flat-plate turbulent boundary layer, the reduction in the viscous wall shear stress is, in general, accompanied by a decrease in the turbulence production or Reynolds stress and, most significantly, by a modification of the near-wall coherent motions. The production and transport of the turbulence are dominated by the formation of well-organized, spatially and temporally dependent wall structures and their interaction with other portions of the flow through a process of gradual lift-up, oscillation, bursting, and ejection in the near-rigid-wall region (Kline *et al.* 1967; Corino & Brodkey 1969; Kim, Kline & Reynolds 1971). Kim *et al.* (1971) further stated that essentially all the turbulence production in the zone $10 < y^+ < 100$ occurs during bursting. Here $y^+$ is the dimensionless position using inner variables, $yu_*/\nu$, where $y$ is distance normal to the surface, $u_*$ is the friction velocity and $\nu$ the kinematic viscosity of the fluid. The production and dissipation of the turbulence reached a maximum in the vicinity of the sublayer edge. Blackwelder & Eckelmann (1979) later suggested that the flow in the sublayer and wall-adjacent regions features counter-rotating pairs of streamwise vortices which dominate the bursting events and the associated turbulence production. The universally accepted value of 0.00041 for the dimensionless bursting frequency $f_b^+$ $(= f_b \nu/u_*^2)$ at $y^+ = 12$ is associated with a dimensionless spanwise wall-streak spacing $\lambda^+$ $(= \lambda u_*/\nu)$ and a dimensionless streamwise coherence length $x_s^+$ $(= x_s u_*/\nu)$ of about 100 and 1000, respectively. It seems, therefore, that a promising candidate for compliant-surface drag reduction would somehow be able to generate a small-amplitude, stable surface response to disrupt this bursting process. Bushnell *et al.* (1977) hypothesized that a successful compliant coating would modulate the 'preburst flow' in the turbulent boundary layer by providing a pressure field that would tend to inhibit or suppress the burst formation. This would result in a reduced number of bursts occurring per unit time and consequently a lower skin-friction drag. It has also been hypothesized that any variation in the magnitude of $\lambda^+$ is accompanied by a change in the skin-friction coefficient $C_f$, defined as $2(u_*/U_0)^{\frac{1}{2}} = 2\tau_w/\rho_f U_0^2$ ($\tau_\omega$ is the viscous shear stress at the wall and $\rho_f$ the density of the fluid).

The correlations among $\lambda^+$, $x_s^+$, $f_b^+$ and $C_f$ have been investigated by researchers elsewhere. Grass (1971) reported that the nature of the interaction between the inner and outer regions remains quite similar whether the wall is smooth or covered with roughness elements protruding up to about 80 wall units ($\nu/u_*$). This may be interpreted as minimizing the importance of wall streaks. On the other hand, experiments on drag reduction by the addition of polymers into the turbulent flow over rigid walls (Donohue, Tiederman & Reischman 1972; Oldaker & Tiederman 1977; Tiederman, Luchik & Bogard 1985) show that there is a direct correlation between increased streak spacing and skin friction reduction. Tiederman *et al.* (1985) further suggested that the effect of the polymer on the flow structure occurs in the range $10 < y^+ < 30$ and that the breakup of low-speed streaks and the subsequent ejection of low-momentum fluid is suppressed (i.e. the bursting rate decreases). On the other hand, Gad-el-Hak *et al.* (1984) reported that no significant differences were observed in the number of recorded streaks and $C_f$ for a PVC plastisol-gel compliant surface in a zero-pressure-gradient flat-plate turbulent boundary layers.

Since the exploration of the near-compliant-wall flow structures offers, in general, only implicit information about the fluid/compliant-surface interaction, explicit information on both the compliant-surface displacement and the turbulent boundary flow field is also needed to better understand the physics of the stable interaction of a passive compliant surface with a turbulent flow. Conventional photographic (Hansen & Hunston 1974; Hansen *et al.* 1980; Gad-el-Hak *et al.* 1984; Gad-el-Hak 1986*a*) and schlieren (McMichael *et al.* 1979) methods have been used to obtain both qualitative and quantitative information on the unstable, large-amplitude, static-divergence waves for a variety of flow conditions. Recently, non-invasive, direct point displacement detectors (Gad-el-Hak 1986; Hess, Peattie & Schwarz 1993) have been developed to measure the instantaneous out-of-plane compliant-surface displacement (larger than about 30 μm) at a chosen point. However, information about the surface displacements on a large section of the compliant surface is needed to link the near-compliant-wall coherent flow structure to the corresponding flow field measurements.

The objective of the present study was to use the hydrogen-bubble technique to determine whether the presence of small-amplitude compliant-surface undulations, in the absence of static-divergence waves, would modify the spatial structure of wall streaks, and whether this modification would lead to any changes in the velocity, turbulence intensity, skin friction, and Reynolds stress measurements, and to any variations in the thickness of the viscous sublayer or the buffer region. Optical holographic interferometry and laser Doppler velocimetry were also utilized to obtain some of the basic parameters of the turbulent boundary layers and the small, whole-field, flow-induced, compliant-surface displacements. These measurements were then linked to the hydrogen-bubble results to better understand the physics of the stable boundary-layer/compliant-surface interaction.

## 2. Experimental apparatus and methods

### 2.1. *Flow facility*

The closed-loop, stainless-steel water tunnel at the National Institute of Standards and Technology (Gaithersburg, Maryland) was used in the present experiments. The test section is 0.6 m in diameter and 3.6 m in length. The contraction ratio is 9 to 1. To

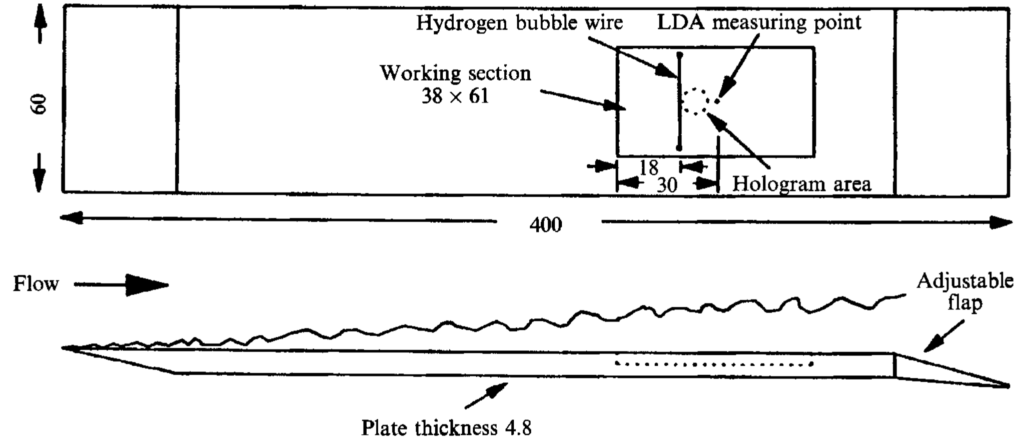

FIGURE 1. Schematic diagram of the experimental set-up; dimensions in cm.

generate a turbulent boundary layer, a stainless-steel flat plate (4.0 m long and 0.6 m wide) is rigidly mounted within the test section along the centreline of the test section (see figure 1). The 4.8 cm thick flat-plate assembly consists of a 6.3 mm highly polished top cover on which a turbulent boundary layer is generated. By adjusting the angle of the tail flap mounted on the downstream end of the plate, a small favourable non-dimensional pressure gradient ($K = (\nu\rho U_0^3)(\mathrm{d}p/\mathrm{d}x) = 0.0126 \times 10^{-6}$ at $U_0 = 1.54$ m/s) was obtained. This small $K$ value has a negligible effect on the measured boundary-layer profiles (Kline *et al.* 1967). The flow conditions tested are listed in table 2 in §3.3.1. Particular emphasis was given to the wall region of the boundary for a Reynolds number based on momentum thickness $R_\theta$ less than 3000.

### 2.2. *Compliant material*

A single-layer isotropic viscoelastic compliant surface was made by mixing commercially available silicone elastometer (Dow-Corning Sylgard 184) and silicone oil (Dow-Corning 200 series silicone oil). The specific gravities of the elastomer and the oil are 1.05 and 0.97 respectively. The mixture was chosen in accordance with Duncan's (1986) theoretical results to produce small-amplitude, stable, compliant-surface displacements which represent the 'footprints' of the flow structure in the shear layer. The amount and viscosity of the oil in the mixture can be varied to change the viscoelastic properties of the compliant material, allowing one to alter the response of the compliant surface to the Reynolds numbers of interest. The compliant surfaces were prepared in a 61 cm long, 38 cm wide and 3.8 cm deep Plexiglas tray which was placed flush in the flat plate. The compliant materials were cured at 175 °F. The leading edge of the compliant surface was located 300 cm downstream of the leading edge of the flat plate. A compliant material with 91% by weight of 100 cSt oil and 9% of elastomer was used in the present experiment. Either black or white, silicone-based colorants (Ferro Corp.), approximately 4.5 and 1.5% by weight, respectively, were added to the mixture to render the original transparent materials opaque for the purposes of photographing (see §2.3 below) or of scattering incident laser light (see §2.4 below). The low-frequency (0.006–1.0 Hz) shear modulus of this compliant mixture was measured with a Weissenberg rheogoniometer, and found to be 2270 dynes/cm$^2$. The damping ratio $\tau$, ($= t_t C_t/d$, where $t_t$ is relaxation time) is 1.64.

### 2.3. *Hydrogen-bubble technique*

Both rigid- and compliant-surface near-wall flow structures were tagged with time lines of bubbles generated using the hydrogen-bubble technique. A simple and inexpensive electronic circuit which followed the design of Budwig & Peattie (1989) was built for delivering high-voltage pulses to the bubble wire. The pulse frequency ($f_p$) was controlled by a function generator, and the pulse width ($t_p$) was set by varying the capacitance ($C_p$) and the resistance ($R_p$) in a capacitor–resistor combination using the $t_p = 0.7R_p C_p$ relation. The electronic circuit can be adjusted for wire voltage as well as pulse frequency and width.

A platinum wire, of diameter 25 μm and length 30 cm, was used as the cathode of the electronic circuit to generate small hydrogen bubbles. The bubble wire was located 18 cm downstream from the leading edge of the compliant surface. The tunnel wall served as the circuit anode. The size of the bubbles generated by the wire are of the order of one-half of the wire diameter, which renders buoyancy effects negligible over the region of interest (Schraub *et al.* 1965). By pulsing the voltage applied to the wire, timelines can be generated. The hydrogen-bubble timelines were made visible by lighting (using three 500 W incandescent bulbs) at an oblique angle of about 45° to the line of sight of the camera. The bubble wire was located parallel to the surface of the flat plate and transverse to the flow direction. Two specially designed hydraulic pistons driven by two separate micrometers (each with a resolution of 25 μm) were built to accurately position the bubble wire. A cathetometer with a maximum resolution of 10 μm was used to determine the distance of the wire above the surface, based on the distance between the wire and its reflection from the surface. This arrangement allowed visualization of the entire boundary layer all the way to the surface of the plate. A 35 mm Nikon camera with a shutter speed set at 4 ms and with the lens aperture set at f2.8 was used to view and record the hydrogen-bubble timelines. Kodak Tmax film (400 ASA) was used, and contact prints made from the photo negatives were used for the measurements of the dimensions of the streaks.

### 2.4. *Optical holographic interferometry*

Holographic interferometry was employed to measure the flow-induced displacements of the compliant surface. A 20 W argon laser (Spectra Physics model 2030) was used as the coherent light source in construction of the holograms and reconstruction of their images. An initial exposure of the compliant surface was made without flow, which gives the reference or comparison surface; then, a second exposure of the undulating surface was made at a specified flow speed. The exposure times were fixed at 1 ms. The reconstructed images were routed to an image digitizer (DT2861) via a CCD camera (Pulnix TM-840) and stored in a frame buffer for surface-displacement determination using an interactive fringe-processing system. Specific topographic features were obtained in the form of interferograms over a surface area 5 cm in diameter. Information about the dimensions of the footprints of the turbulence on the compliant surface were obtained in the form of line contours and three-dimensional display of the surface displacements. Details of the optical arrangement and the determination of compliant-surface displacements from the interferograms are given in Lee, Fisher & Schwarz (1993).

### 2.5. *Laser Doppler velocimetry*

Mean-velocity, turbulence intensity, and Reynolds stress measurements were made with a two-component, fibre-optic laser Doppler anemometer (LDA). A 4 W argon-ion laser yielding 1.6 W and 1.1 W of power at wavelengths of 514 and 488 nm,

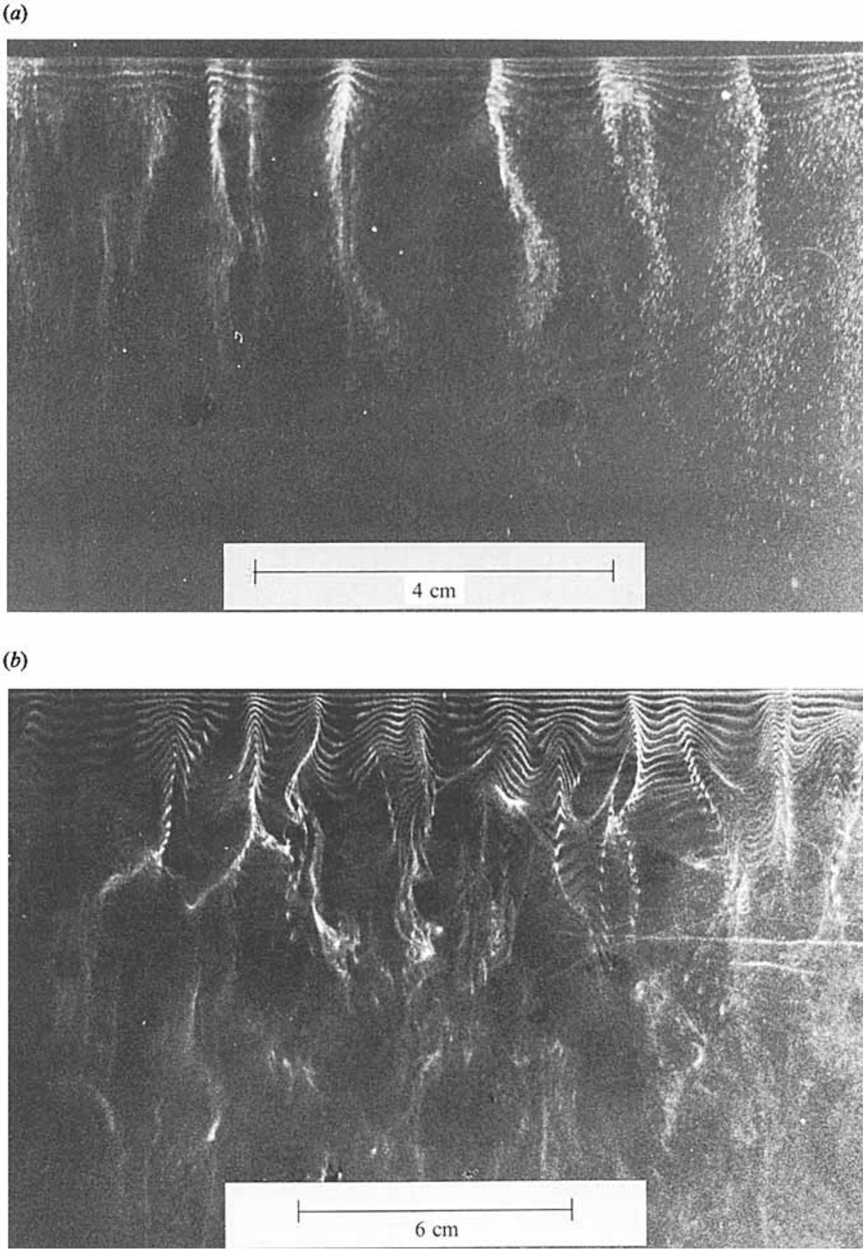

FIGURE 2(*a*, *b*). For caption see facing page.

respectively, was used for the LDA system. A beam expander (Dantec 55 × 12) and a transmitting lens (Dantec 55 × 57) were also integrated into this LDA system to allow measurements along the centreline of the plate. The measuring volume is 75 μm in diameter and 0.63 mm in length. The beam expander and probe head (Dantec 60 × 11) combination was mounted on a specially built traversing mechanism (with four degrees of freedom and a resolution of 1 μm) to measure the turbulent flow field along the surface of interest. This combination was also positioned at an angle of 1° (pointing

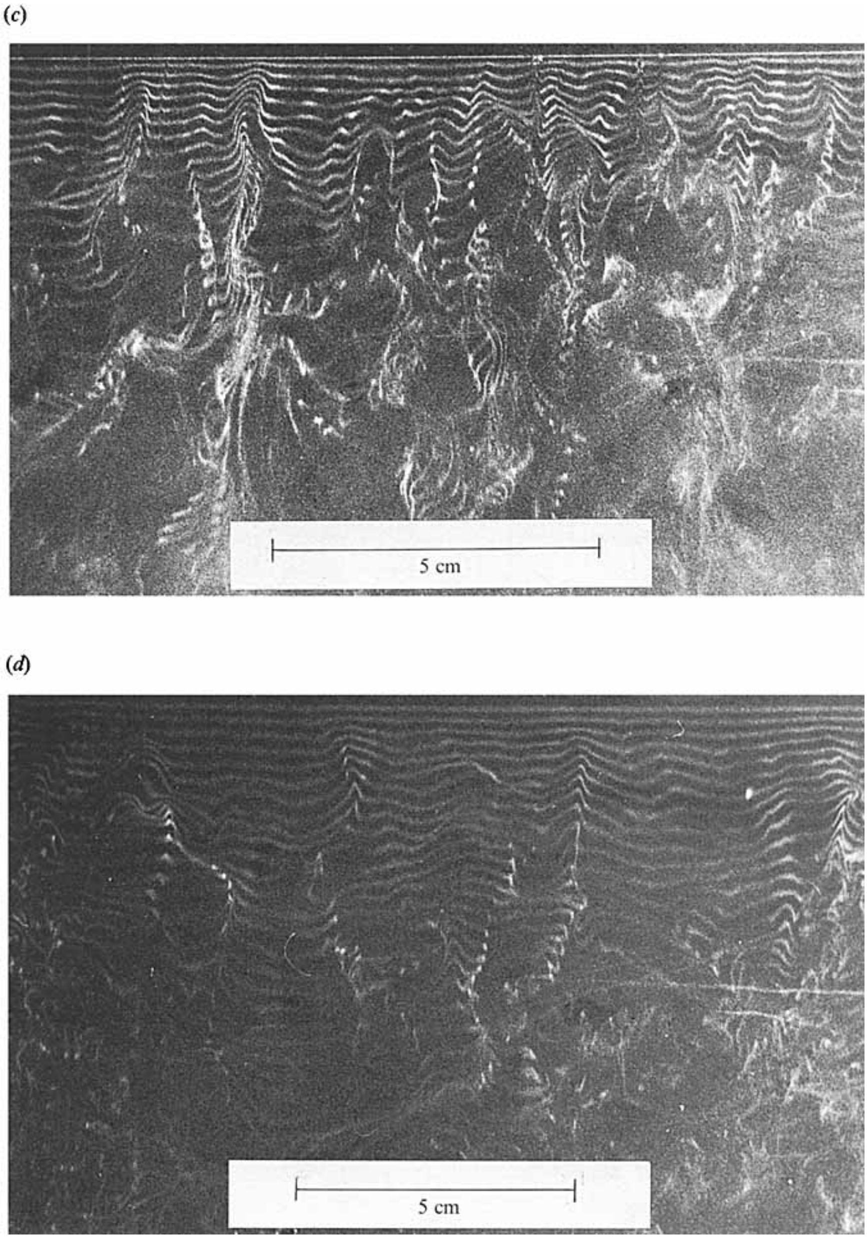

FIGURE 2. Plan views of low-speed streaks over a rigid-surface flat-plate turbulent boundary layer. (*a*) $y^+ = 2, f_p = 40$ Hz and $R_\theta = 897$; (*b*) $y^+ = 9, f_p = 80$ Hz and $R_\theta = 897$; (*c*) $y^+ = 35, f_p = 40$ Hz and $R_\theta = 1348$; and (*d*) $y^+ = 185, f_p = 40$ Hz and $R_\theta = 1348$.

toward the plate), which minimized interference between the plate and laser beams, thereby allowing velocity measurements as close as 0.04 mm to the plate. Scattered light was collected in the backward direction.

For Reynolds stress measurements, a specially designed beam-path displacer was used to convert the four-beam system into a three-beam setup. The probe head was rotated 45° to the mean flow direction so that the three-beam system could be traversed as close to the wall as possible. Also, to ensure that measurements on both channels

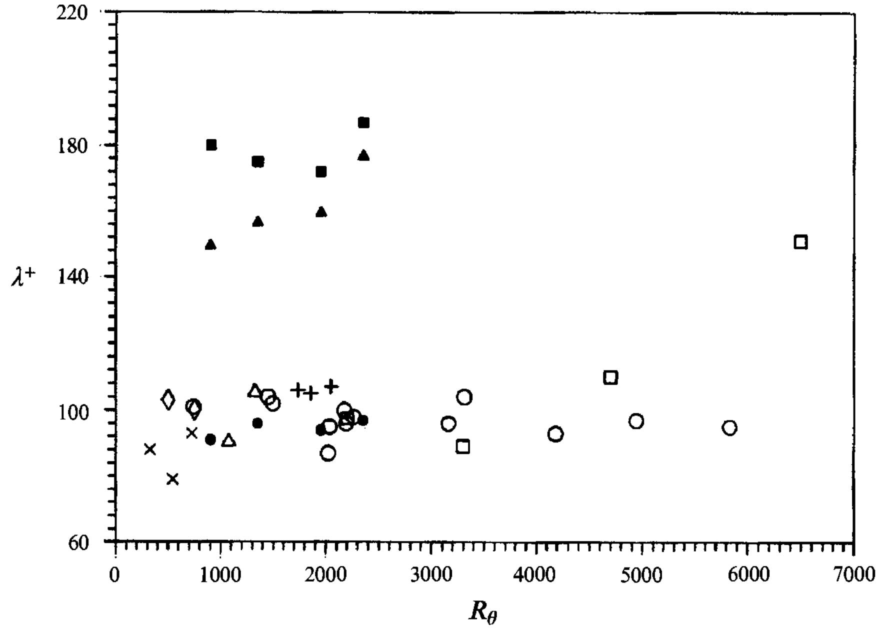

FIGURE 3. Variations of mean dimensionless spanwise wall-streak spacing with Reynolds number. △, Kline *et al.* (1967), $y^+ = 4$; □, Gupta *et al.* (1971), $y^+ = 2–7$; +, Lee *et al.* (1974); ×, Achia & Thompson (1976); ◇, Nakagawa & Nezu (1981), $y^+ = 4$; ○, Smith & Metzler (1983), $y^+ = 5$. Present measurements: ●, rigid surface, $y$, $y^+ = 2–6$; ▲, compliant surface, $y^+ = 3–7$ (based on $u_*$ obtained from rigid-surface mean-velocity measurements); ■, compliant surface (based on $u_*$ obtained from compliant-surface mean-velocity measurements).

were obtained from the same particle, data were taken in the coincidence mode. The instantaneous streamwise and normal velocity components were decomposed from the direct velocity measurements using a standard rotation of axes (see Walker & Tiederman 1990). The Reynolds stress at selected $y$-locations was obtained from signal points at evenly spaced time intervals. The velocities corresponding to each evenly spaced time step were calculated by linear interpolation between adjacent points in the decomposed raw velocity signals (see Wei & Willmarth 1989).

Two Dantec 57N10 burst spectrum analysers (BSA), each equipped with a BSA frequency shift module (Dantex 57N14), were used to analyse the Doppler signals. The data were acquired and processed by a personal computer using the software named BURSTware. The computer-controlled BSA is capable of working in conditions of poor seeding, i.e. low signal-to-noise ratio (SNR), and in conditions of severe reflections from nearby surfaces. The SNR threshold is about 15 dB lower than that of a conventional burst counter. This means that bursts of small particles, which are usually buried in the signal noise, can now be 'seen'. About 6000 samples per second were taken for each measurement point for most flow conditions. The confidence intervals were about 0.2 % on the mean velocity and 2 % on the turbulence intensities. The deionized water flow was seeded with silicone carbide particles (TSI Model 10081) with a mean diameter of 1.5 μm and a refractive index of 2.65.

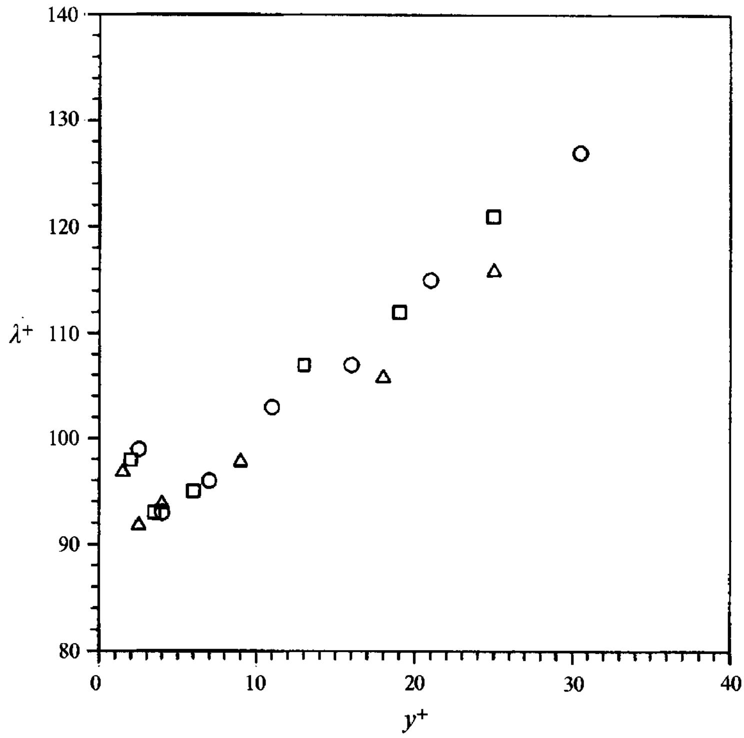

FIGURE 4. Mean dimensionless spanwise wall-streak spacing as a function of distance from wall. ○, $R_\theta = 2347$; □, $R_\theta = 1952$; △, $R_\theta = 1348$.

## 3. Results and discussion

### 3.1. *Near-wall flow structures*

The near-wall flow structures were visualized using hydrogen-bubble timelines at $R_\theta = 2347$, 1952, 1348 and 897. Plan-view pictures of the spanwise low-speed wall streaks at different locations above both the rigid and compliant surfaces are presented with the flow direction from top to bottom.

### 3.1.1. *Rigid-surface case*

Figure 2 summarizes the low-speed wall-streak structures observed in the present investigation at various $R_\theta$. The present observations are consistent with those of previous investigators using the hydrogen-bubble technique (e.g. Kline *et al.* 1967; Lu & Smith 1991; and others). Figure 2(*a*) shows the low-speed wall-streak flow structure in the viscous sublayer. The collection of the hydrogen bubbles into a streaky structure is characteristic of this region. The presence of streaks is a sufficient condition for establishing whether a given boundary-layer flow is turbulent. Figure 2(*b*) shows that the streaks become less noticeable in the buffer region. Figure 2(*c*) shows the flow structure in the log region. The streaks become less visible as compared to those shown in figures 2(*a*) and 2(*b*). Figure 2(*d*) shows the flow structure in the wake region.

Figure 3 shows a collection of all the data available on the values of the mean dimensionless spanwise spacing of the wall streaks using the hydrogen-bubble technique at different $R_\theta$. The present observed $\lambda^+$ values are in good agreement with the values given by Kline *et al.* (1967) and those obtained by nearly all subsequent investigators. A mean value of $\lambda^+$ of 95 for $y^+ = 2$–6 was found from the present study.

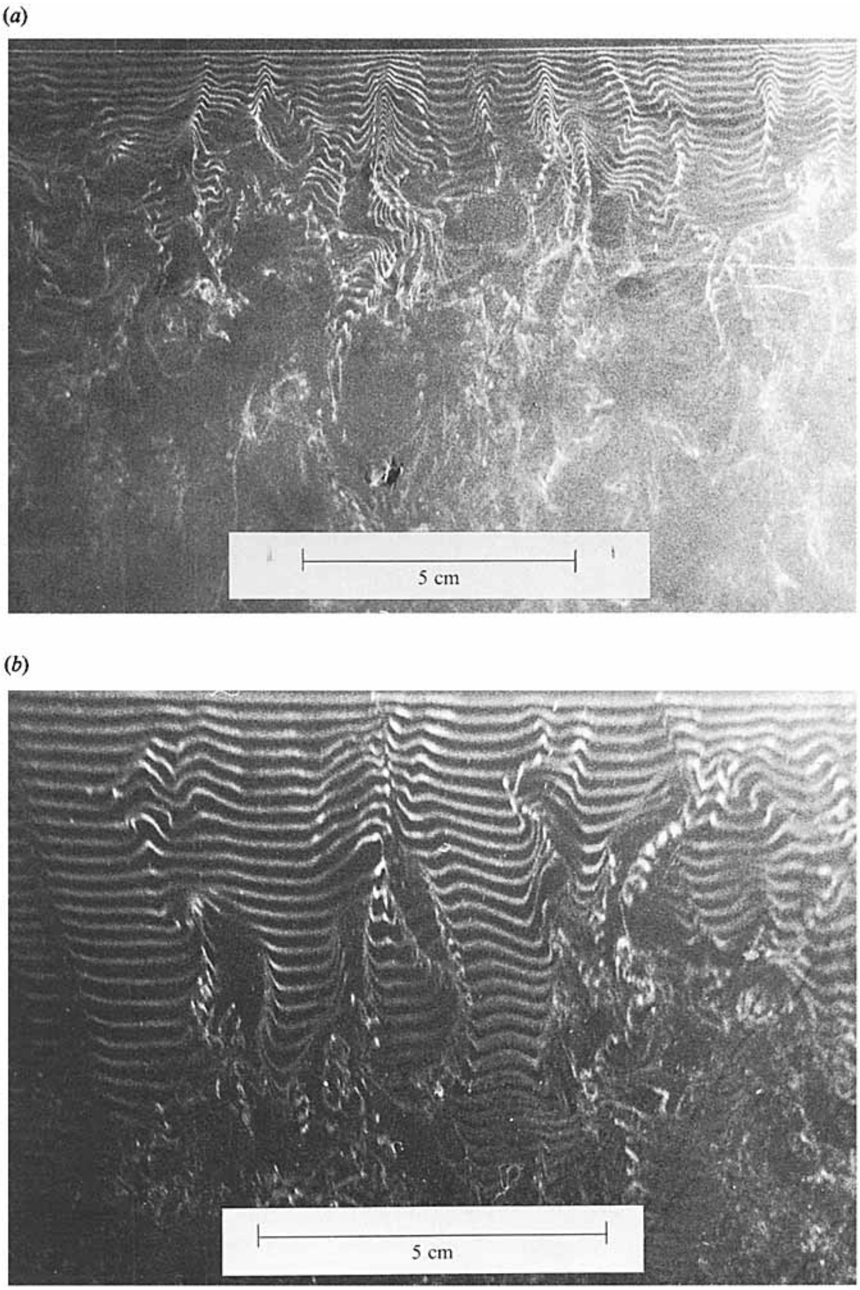

FIGURE 5(*a*, *b*). For caption see page 384.

Figures 2 and 3 also show clearly that low-speed streaks are essentially invariant with $R_\theta$.

Figure 4 shows the variation of spanwise wall-streak spacing with the distance above the surface for $y^+ < 30$. Results show that $\lambda^+$ increase with $y^+$ (for $y^+ > 6$). For $6 < y^+ < 30$, the streaks begins to merge, which causes a larger wall-streak spacing. Apparently, the merging events are the result of small stretched and lifted vortex loops generated in the near-wall region. These vortex loops interact strongly with each other

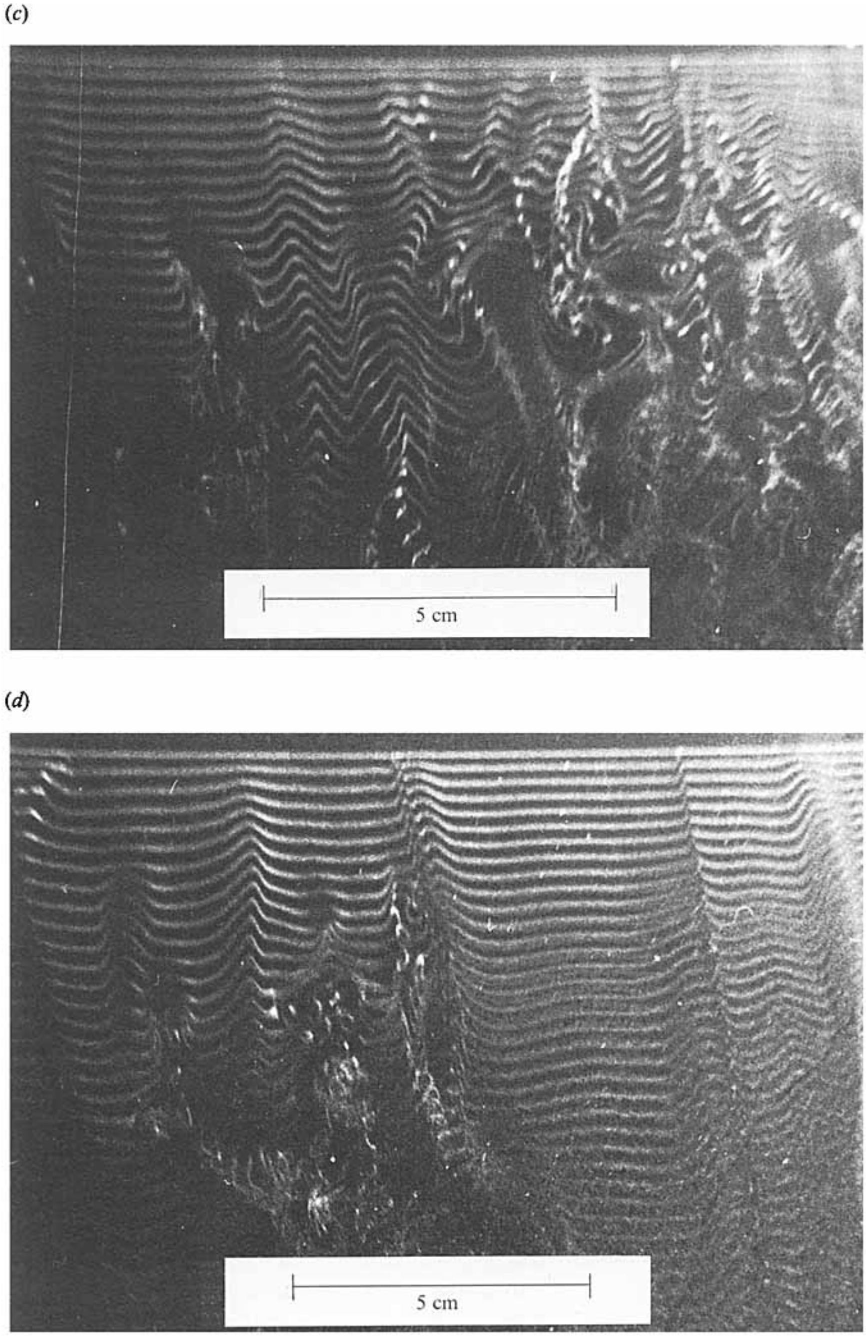

FIGURE 5(*c*, *d*). For caption see page 384.

(e)

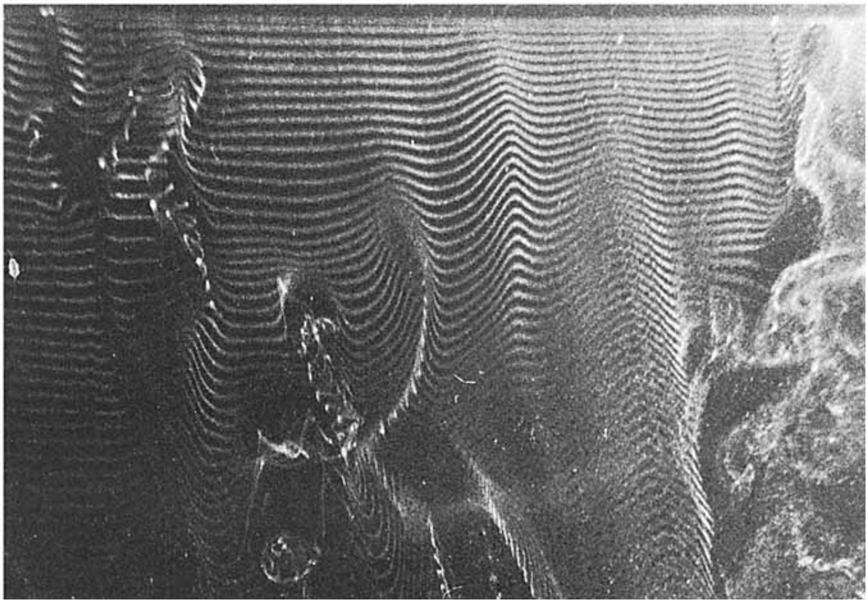

FIGURE 5. Plan views of intermittent laminar-like flow structures at $R_\theta = 1348$ and $f_p = 40$. (a) Rigid surface case at $y^+ = 51$. Compliant surface cases at $y^+ = 49$ at four different times (note the time intervals are not constant): (b) at time $t_1$, (c) $t_2$, (d) $t_3$, and (e) $t_4$.

as they move away from the wall. This merging and interacting behaviour is most pronounced for $10 < y^+ < 30$, i.e. in the buffer zone region, which accounts for the major turbulence production in a flat-plate turbulent boundary layer.

### 3.1.2 *Compliant-surface case*

Visual observations of the flow structure over the compliant surface generally showed a similar low-speed wall-streak appearance compared to the rigid-surface case, but with larger values of $\lambda^+$ (as indicated by the solid triangles and solid squares in figure 3). Solid triangles and squares shown in figure 3 indicate the values of the compliant-wall-streak spacings which were non-dimensionalized by the friction velocity obtained from the rigid- and compliant-surface cases, respectively. Also, the compliant-wall streaks appear to be more quiescent. More interestingly, an intermittent laminarization-like flow phenomenon over the particular compliant surface was observed at lower Reynolds numbers. This phenomenon is most significant for the lowest $R_\theta$ (= 897) investigated in the present study. The increase in the $\lambda^+$ under the influence of surface compliance or undulations is accompanied by a decrease in the wall shear stress which will be further discussed in †3.3. below.

Figure 5 shows the intermittent laminarization-like phenomenon over the particular compliant surface observed at $R_\theta = 1348$. The bubble wire was located at $y^+ = 49$ and pulsed at $f_p = 40$ Hz. The free-stream velocity was measured with the LDA system to ensure a steady-state flow condition. Apparently, there is a stable interaction taking place between the present particular compliant surface and the turbulence flow field. This interaction becomes more significant with decreasing $R_\theta$ (see figure 6–8 below). Figures 5(*b*), 5(*c*), 5(*d*) and 5(e) show the plan views of the near-wall flow structure over the compliant surface at four different time sequences. The time intervals were

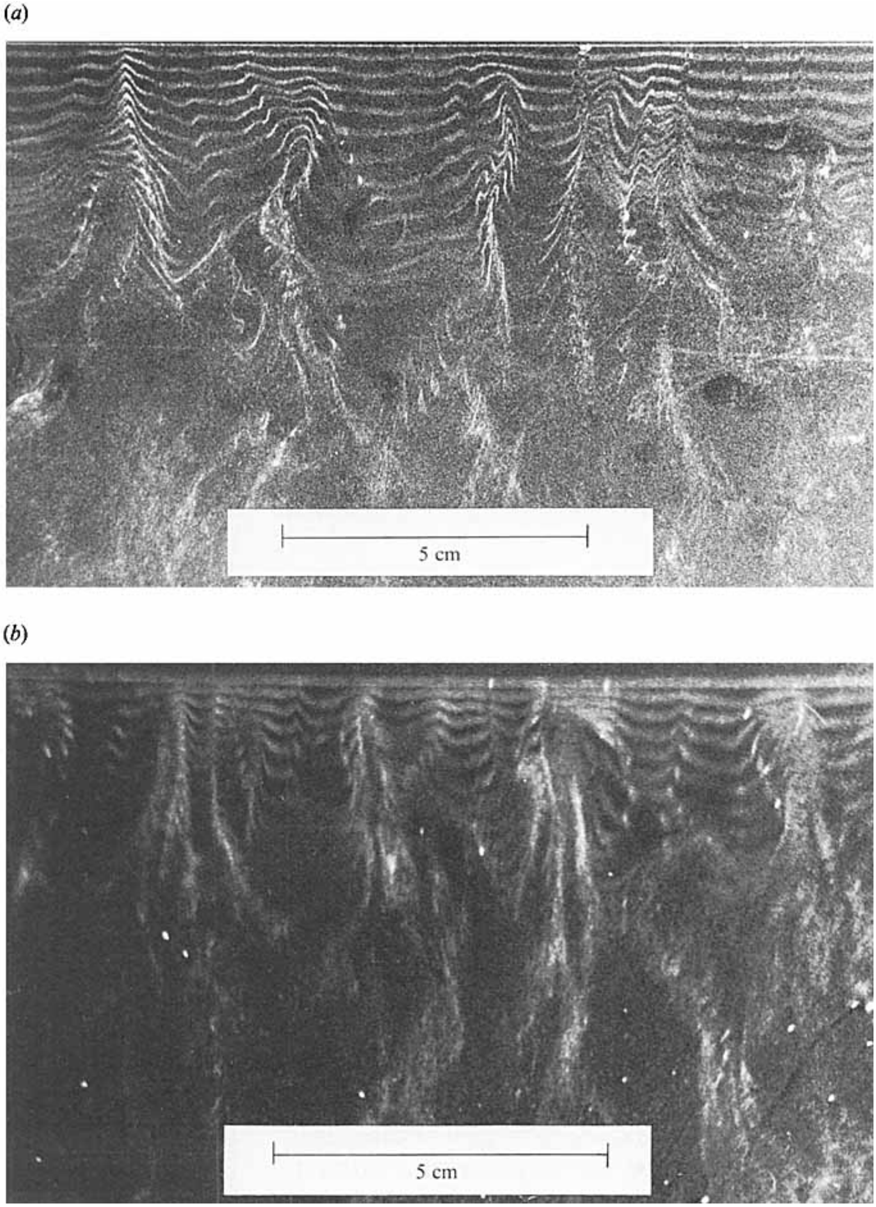

FIGURE 6(*a*, *b*). For caption see page 387.

sequential but arbitrary. The corresponding rigid-surface near-wall flow structure is shown in figure 5(*a*) at $y^+ = 51$. Figure 5 shows that at time $t_1$ large scales of motions are more evident (which is similar to figure 5(*a*) than at the following times $t_2$, $t_3$ and $t_4$. The flow structure became more (quasi-) laminar-like, or quiescent, as time elapsed. The laminar-like patches were observed typically for 5–10 s intervals, and had a duration of 1–2 s. The observed relaminarization of a turbulent boundary layer implies that this particular compliant surface seems to effect a change in the balance between the turbulence production and dissipation, and to exert a large net influence on the turbulence as a whole. The instantaneous surface displacements are shown in figure 10 below in §3.2.

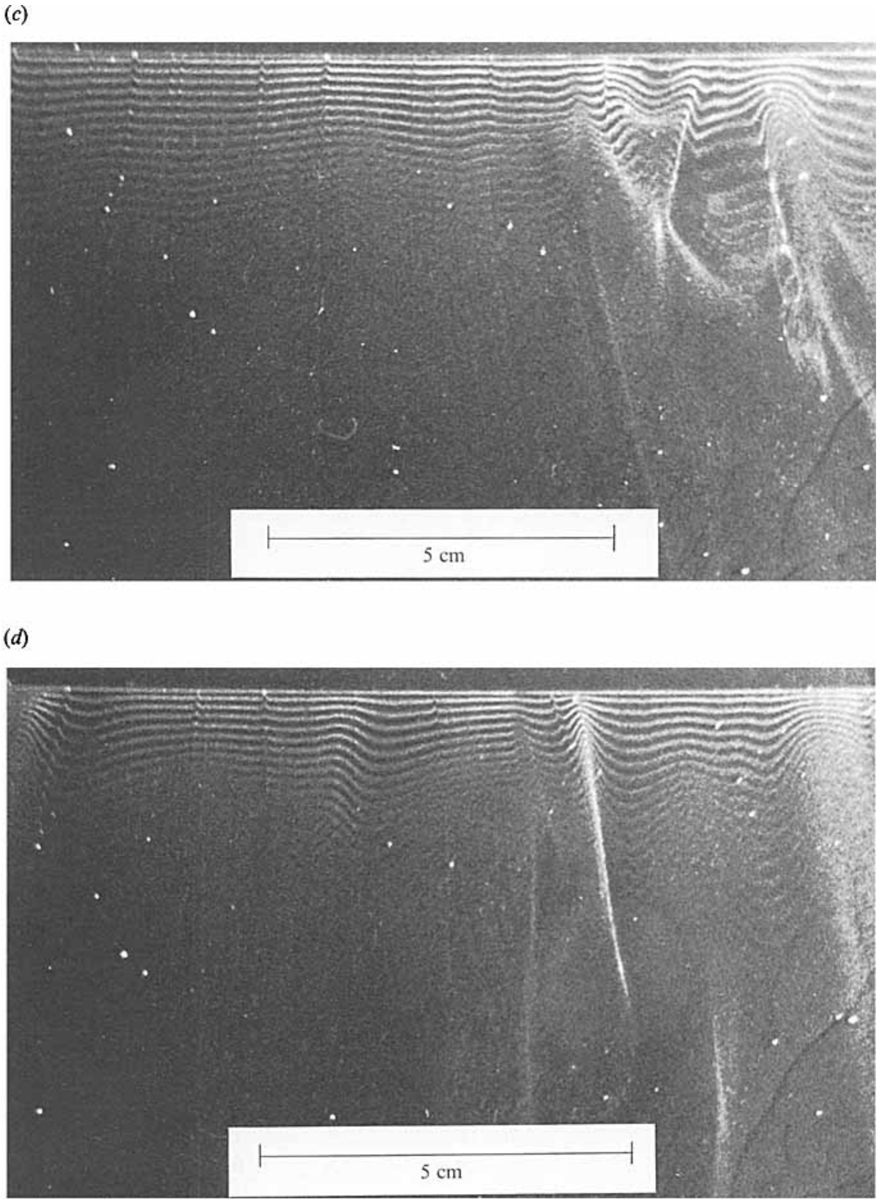

FIGURE 6(*c*, *d*). For caption see facing page.

Figures 6, 7 and 8 show the intermittent laminarization-like flow structures caused by the stable fluid/compliant-surface interaction at three different wire positions (i.e. $y^+ = 17, 20$ and 26) for $R_\theta = 897$ and $f_p = 20$ Hz. Figure 6(*a*) shows the corresponding rigid-surface flow structure at $y^+ = 26$ for $f_p = 20$ Hz. Figure 6(*b–e*) shows the onset and the end of the laminar-like flow phenomenon from time $t_1$ to time $t_4$ at $y^+ = 17$. The laminar-like flow structure only appeared for a short period of time (figures 6*c* and 6*d*) and returned to normal conditions (figures 6*e* and 6*b*). The surface displacements are shown in figure 9 below in §3.2. Similar laminar-like observation was found for $y^+ = 20$ at three different time sequences (figures 7*a–c*). Figure 8 shows the plan views

(*e*)

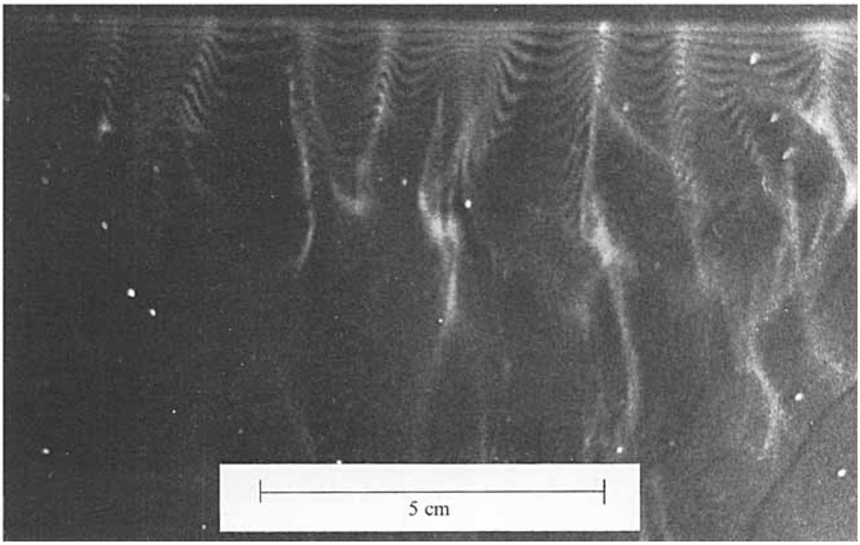

FIGURE 6. Plan views of intermittent laminar-like flow structures at $R_\theta = 897$. (*a*) Rigid surface case of $y^+ = 17$ and $f_p = 40$ Hz. Compliant surface cases at $y^+ = 17$ and $f_p = 20$ Hz at four different times (note the time intervals are not constant): (*b*) at time $t_1$, (*c*) $t_2$, (*d*) $t_3$ and (*e*) $t_4$.

of the near-compliant-wall flow structures at $y^+ = 26$. Figure 8(*b*) shows that at time $t_2$ the flow structure became quiescent or laminar-like from an original turbulent boundary-flow condition.

### 3.2. *Compliant-surface displacements.*

Double-exposure holograms were recorded at $R_\theta = 897$, 1348, 1952, and 2347. The centres of these holograms were located 2.5 cm downstream from the bubble wire. The normalization dimension is 5 cm. The flow direction is from left to right.

Figure 9(*a*) is a photograph of the reconstructed interferogram on a compliant surface from a double-exposure hologram at $R_\theta = 897$. Figure 9(*b*) shows the three-dimensional display or topography of the flow-induced surface displacements. The peak-to-valley surface displacement ($d_{pv}$) is 1.67 μm and the r.m.s. value ($d_{rms}$) is 0.32 μm. Figure 10(*a*) shows the interferogram with a second exposure at $R_\theta = 1348$. More complicated and closed-ring fringes are seen in figure 10(*a*) as compared to figure 9(*a*), which indicates that the magnitude of the compliant-surface deformation induced by the random forcing of the turbulence field increases with $R_\theta$. Figure 10(*b*) shows the three-dimensional display of the measured compliant-surface displacement of figure 10(*a*) with $d_{pv}$ and $d_{rms}$ equal to 2.93 μm and 0.58 μm, respectively. Figures 11(*a*) and 11(*b*) show the photograph and the corresponding surface displacements of the reconstructed interferogram at $R_\theta = 1952$. The value of $d_{pv}$ and $d_{rms}$ were found to be 3.82 μm and 0.72 μm, respectively.

### 3.3. *Turbulent-boundary-layer characteristics*

Time-mean velocity, turbulence-intensity, and Reynolds stress were measured for $897 < R_\theta < 8649$ at $x = 330$ cm, $x$ being downstream distance from the plate leading edge. The mean-velocity profiles obtained were then employed to determine $\delta$, $\theta$, and $u_*$ (using Clauser's cross-plot method, the wall-slope method, and Reynolds stress

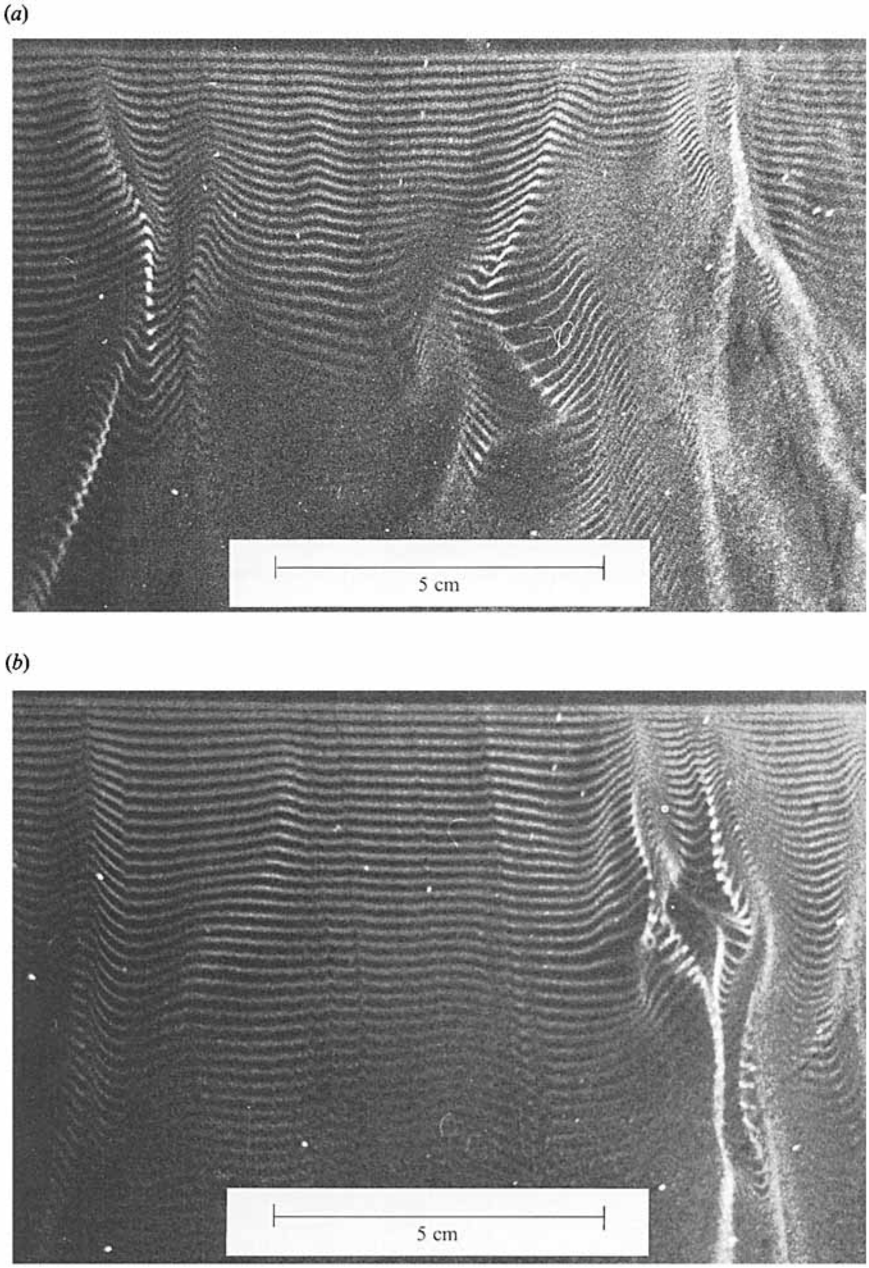

FIGURE 7$(a, b)$. For caption see facing page.

measurements, separately). The subsequent data were fitted to appropriate empirical correlations, and these correlations were used to establish the parameters for the visual studies.

### 3.3.1 *Rigid-surface case*

Figure 12 shows the mean-velocity profiles using wall variables, $u^+ = u/u_*$, at seven different $R_\theta$. The non-dimensionalized parameter $u_*$ was obtained using Clauser's (1956) cross-plot method. Results show that the law-of-the-wall is independent of

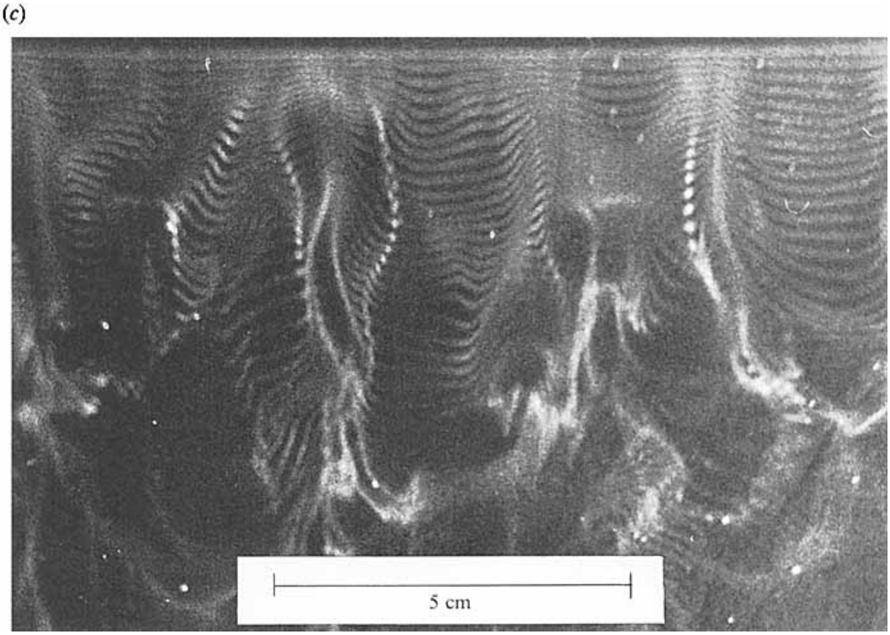

FIGURE 7. Plan views of intermittent laminar-like flow structures over the present compliant surface at three different times for $R_\theta = 897$. The bubble wire is located at $y^+ = 20$ and pulsed at $f_p = 20$ Hz (note the time intervals are not constant): (*a*) at time $t_1$, (*b*) $t_2$, and (*c*) $t_3$.

Reynolds number but the extent of the logarithmic region was found to decrease with decreasing $R_\theta$. In other words, any variation of the turbulent boundary layer with Reynolds number is entirely limited to the outer region of the flow. Also, the maximum value of the wake deviated from the equilibrium boundary layer (i.e. for $R_\theta > 5000$) $\Delta U^+$ did not disappear (see figure 12 for definition). The existence of a turbulent boundary layer at the lowest $R_\theta$ ($= 897$) investigated in the present study is assured by comparing this value to the minimum $R_\theta$ determined by investigators elsewhere (see table 1). The existence of the turbulent boundary layer at $R_\theta = 897$ can also be demonstrated from the visual observations shown in figure 2(*a*). The variation of the skin-friction coefficient with the Reynolds number is shown in figure 13. The present $C_f$ measurements are a little larger than the data (indicated by open squares) of Purtell, Klebanoff & Buckley (1981) and Coles's (1962) proposed values (dashed line). The increase in the present $C_f$ measurements may be attributed to the effect of the relatively high background free-stream turbulence intensity level. Coles (1962) suggested that an increase in free-stream turbulence decreases the strength of the wake component and thus increase the local $C_f$ at a fixed $R_\theta$.

Figure 14 shows the streamwise turbulence-intensity profiles at four different $R_\theta$. Results show that the peak in the turbulence intensity profile increased with decreasing $R_\theta$ compared to the values of equilibrium conditions (dashed line) from Klebanoff (1953). This tendency is consistent with the measurements of Purtell *et al.* (1981) and Erm & Joubert (1991), except that LDA turbulence data are slightly higher than hot-wire measurements (Buchhave, George & Lumley 1979). The increase in the r.m.s. value of the velocity fluctuation may primarily reflect suppression of all but the largest scales in the turbulence as the Reynolds number is reduced.

Figure 15 shows the Reynolds stress measurements as a function of the distance from

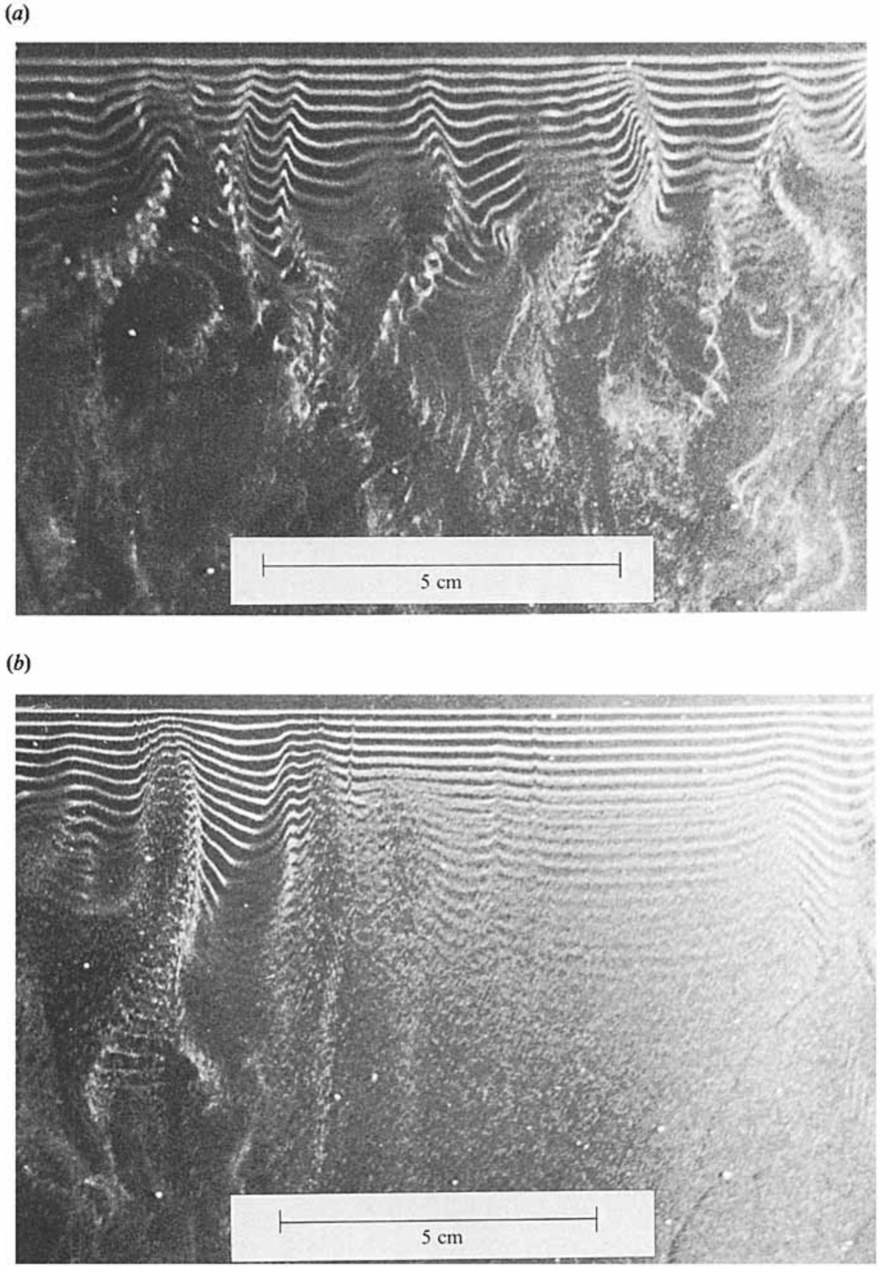

FIGURE 8. Plan views of intermittent laminar-like flow structures over the present compliant surface at two different times for $R_\theta = 897$. The bubble wire is located at $y^+ = 26$ and pulsed at $f_p = 20$ Hz: (*a*) at time $t_1$, and (*b*) $t_2$.

the wall at three different $R_\theta$. This figure indicates that the magnitude of the Reynolds stress depends on $R_\theta$, but the extent of the dependency varies throughout the $y/\delta$ range. Klebanoff's (1953) measurements at high Reynolds number are also plotted (dashed line) in this figure. The variation of the profiles with $R_\theta$ is greatest near the wall, but diminishes with decreasing $y/\delta$. Table 2 summarizes the friction velocities obtained

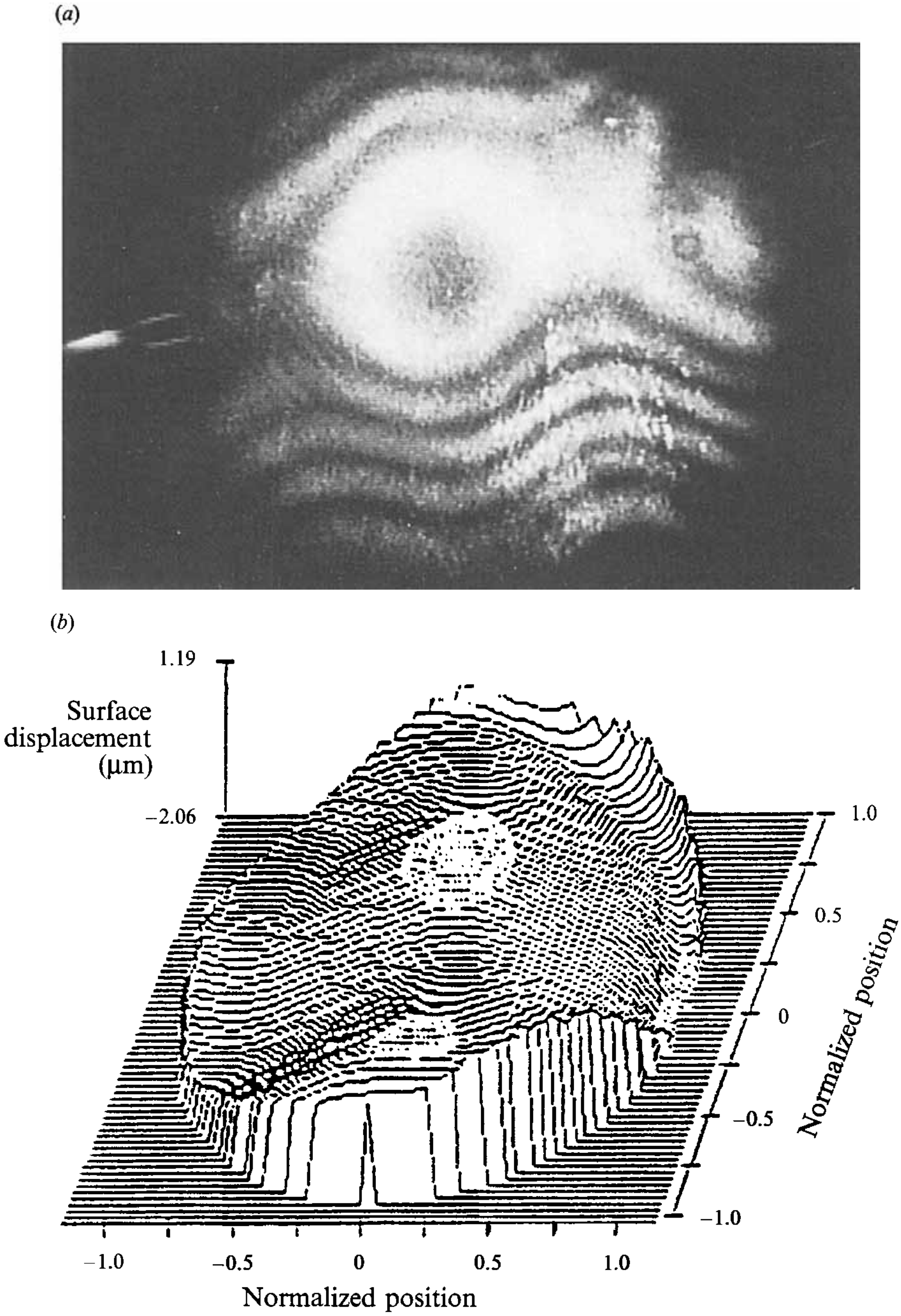

FIGURE 9. (*a*) Photograph of the reconstructed interferogram and (*b*) three-dimensional display of the surface displacements at $R_\theta = 897$.

from the present investigation. The $C_f$ determined by the wall-slope method differed somewhat from those determined by the cross-plot method and the Reynolds stress measurements. A difference of $-7\%$ to $-12\%$ in $C_f$ extrapolated from the Reynolds-stress data was found compared to the value determined by the wall-slope method.

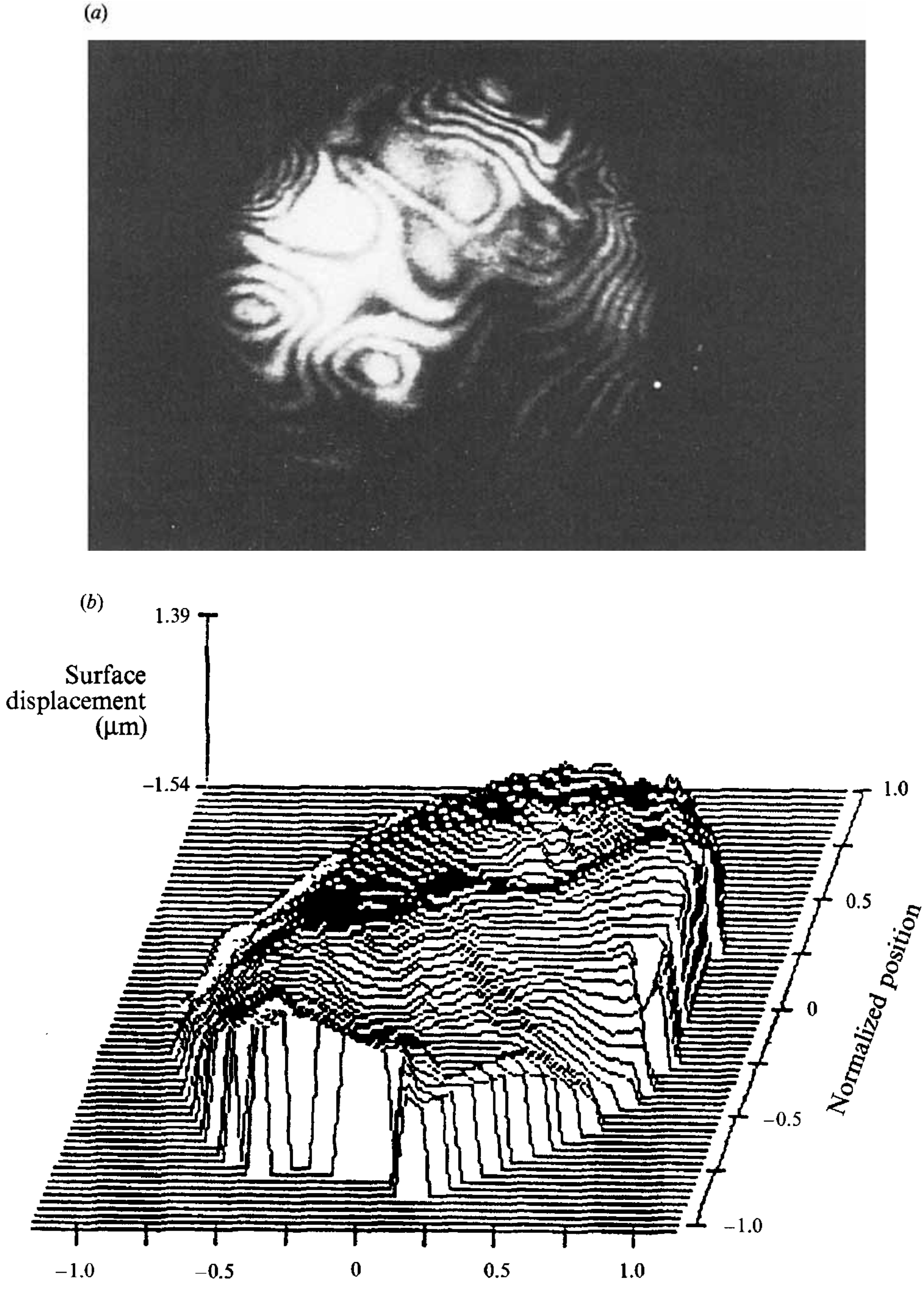

FIGURE 10. (*a*) Photograph of the reconstructed interferogram and (*b*) three-dimensional display of the surface displacements at $R_\theta = 1348$.

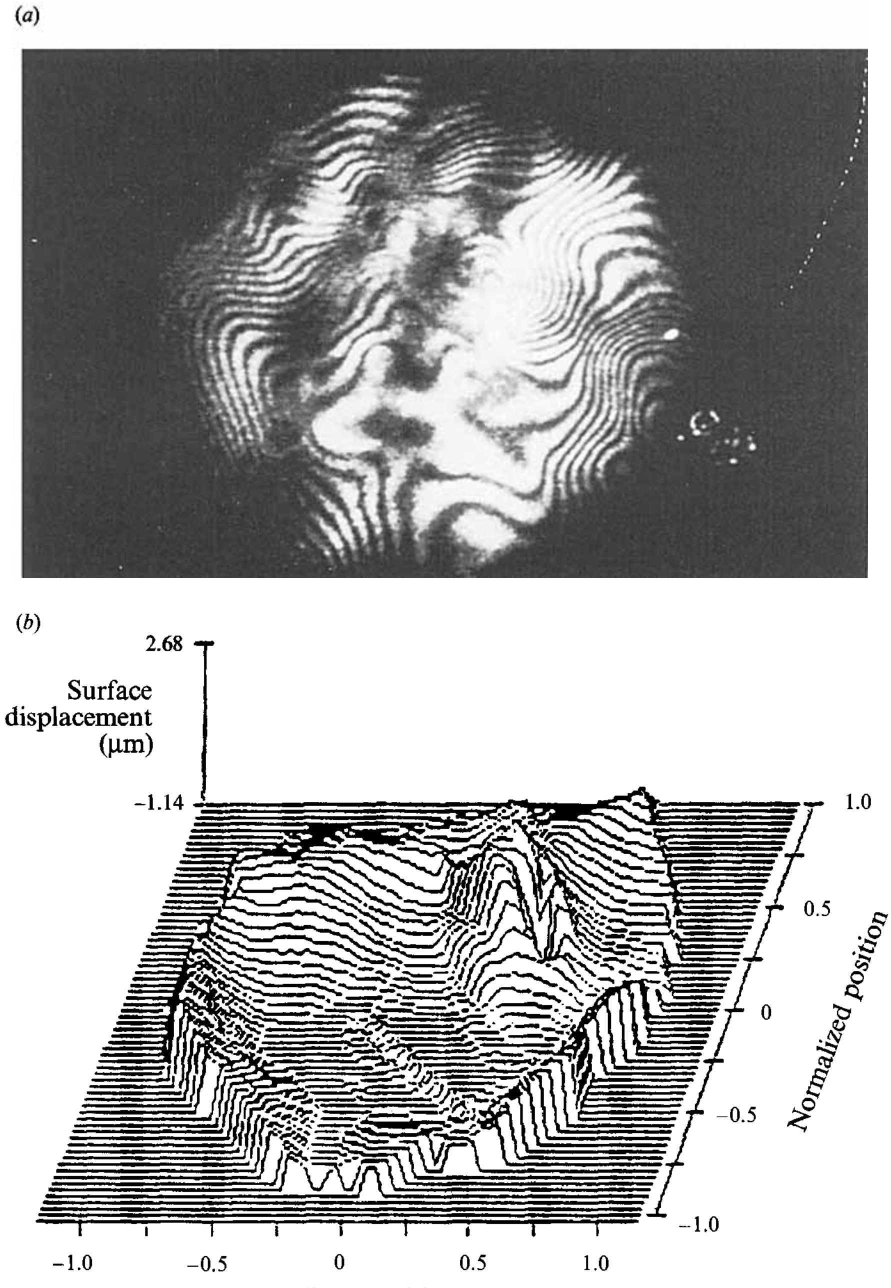

FIGURE 11. (*a*) Photograph of the reconstructed interferogram and (*b*) three-dimensional display of the surface displacements at $R_\theta = 1952$.

This discrepancy may be attributed to the accuracy of the linear-interpolation data-reduction method as described in §2.5 and to the spatial resolution of the measuring volume of the present LDA system (see Johnson & Barlow 1989). Johnson & Barlow reported that for high data density, Reynolds stress profiles in the near-wall region

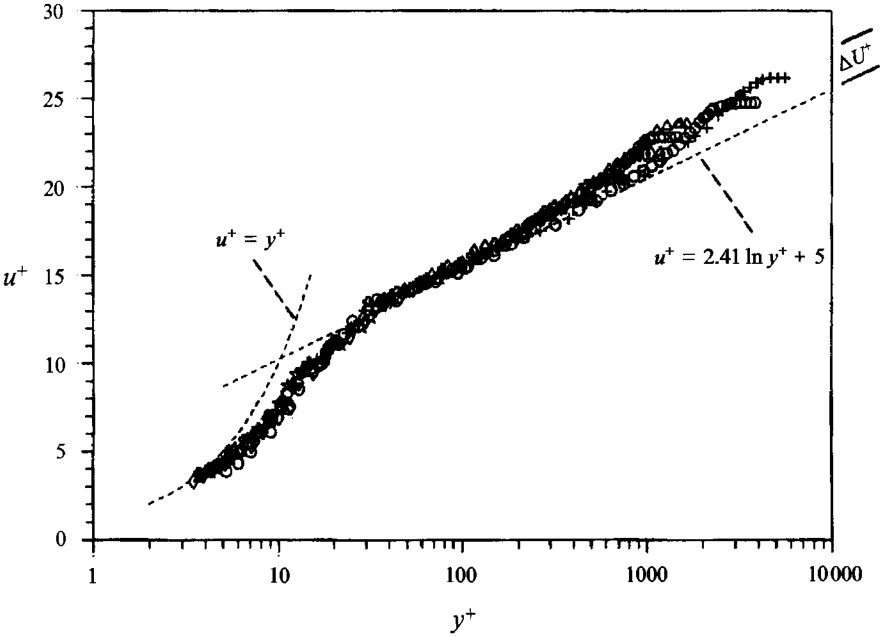

FIGURE 12. Mean velocity profiles in semi-logarithmic coordinates at seven different Reynolds numbers: ----, Clauser (1956); present measurements: +, $R_\theta = 8650$; ○, $Re_\theta = 6200$; △, $R_\theta = 2850$; ×, $R_\theta = 2347$; ◇, $R_\theta = 1952$; ☆, $R_\theta = 1348$; ✙, $R_\theta = 897$.

| Investigators | $R_\theta$ |
|---|---|
| Smits *et al.* (1983) | 354 |
| Preston (1958) | 389 |
| Purtell *et al.* (1981) | 465 |
| Coles (1962) | 500 |
| Erm & Joubert (1991) | 581 |
| Murlis *et al.* (1982) | 700 |
| Granville (1977) | 738 |

TABLE 1. Summary of the minimum Reynolds number for a zero-pressure-gradient flat-plate turbulent boundary layer

strongly depend on the measuring volume length; at a given $y$-position, Reynolds stress decreases with increasing measuring volume length. Uncertainties of $-10\%$ to $+25\%$ in the values of Reynolds stress were detected due to the present of multiple seed particles in the measuring volume.

### 3.3.2. *Compliant-surface case*

Figure 16(*a–f*) shows comparisons of the mean-velocity profiles of the compliant-surface case (open squares) with that of rigid-surface case (solid squares) at six different $R_\theta$. All these point-velocity measurements were made with the absence of static-divergence waves. The lowest $R_\theta$ for the hydroelastic instabilities to appear is about 11000 for the present compliant surface. The compliant-surface mean-velocity data were non-dimensionalized by the friction velocities obtained using the wall-slope method. Results show that the compliant-surface mean-velocity profiles had well-defined logarithmic and wake regions, but with a shift in the log-wall region at low $R_\theta$ (see figures 16*c*, 16*d*, and 16*e*). The magnitude of this shift increases with decreasing

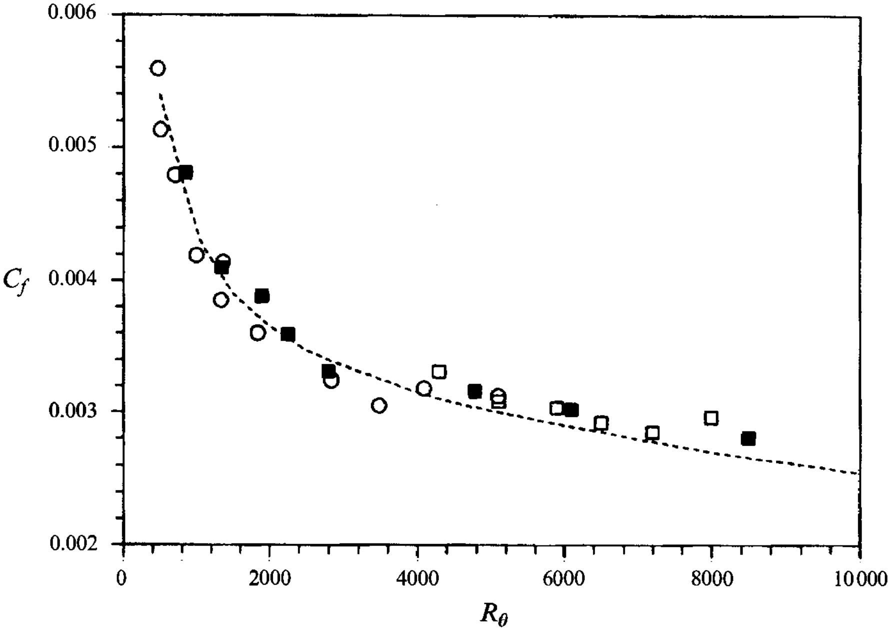

FIGURE 13. Variation of skin-friction coefficient with Reynolds number. ----, Coles (1962); □, Purtell *et al.* (1981); ○, Hess (1990); ●, present measurements.

Reynolds number. The shift in the compliant-surface log-wall region at low $R_\theta$ is accompanied by: (i) a slightly broadened buffer region and viscous sublayer (figures 16*c*, 16*d*, and 16*e*); (ii) a lowered $u_*$ or $C_f$ (table 2); and (iii) an increased value of $\lambda^+$ compared to the corresponding rigid-surface measurements (figure 3). Figure 16(*c–f*) together with the visual results (figures 2–8) suggest that the mean-velocity flow fields were altered due to the stable interaction of the particular compliant surface with the turbulence flow field. Apparently, the formation of the low-speed wall streaks is suppressed by the presence of the compliant surface undulations which in turn yield a lower $C_f$. In other words, the vortex stretching which is responsible for the transfer of turbulent energy and vorticity is modulated by the surface compliance or the stable fluid/compliant-surface interaction. However, the physical mechanism responsible for this favourable interaction of the compliant surface with the fluid is still not understood. No significant changes in the compliant-surface $(u^+, y^+)$ profiles (see figures 16*a* and 16*b*) were found compared to the corresponding rigid-surface measurements as the Reynolds number approaches or becomes larger than the value for the equilibrium conditions.

The present compliant-surface mean-velocity and $C_f$ measurements differ with the results of Gad-el-Hak *et al.* (1984) under similar conditions. No modification of the turbulence was reported by these investigators. Gad-el-Hak *et al.* found that the mean-velocity and the r.m.s. velocity fluctuation measurements for a turbulent boundary layer over the compliant surface did not differ from that on a rigid surface as long as the static-divergence waves were absent. Also, no significant differences were observed in the number or the length of recorded streaks. The compliant material used by Gad-el-Hak *et al.* was a plastisol gel made by heating to 160 °C a mixture of polyvinyl chloride resin (PVC), dioctyle phthalate (plasticizer), and dibutyl tin maleate (stabilizer). The $G$ and $d$ were varied in the range 50–125000 dyne/cm$^2$ and 0.5–7 mm, respectively. The displacement-thickness Reynolds numbers investigated in their experiments ranged from 400 to 6000.

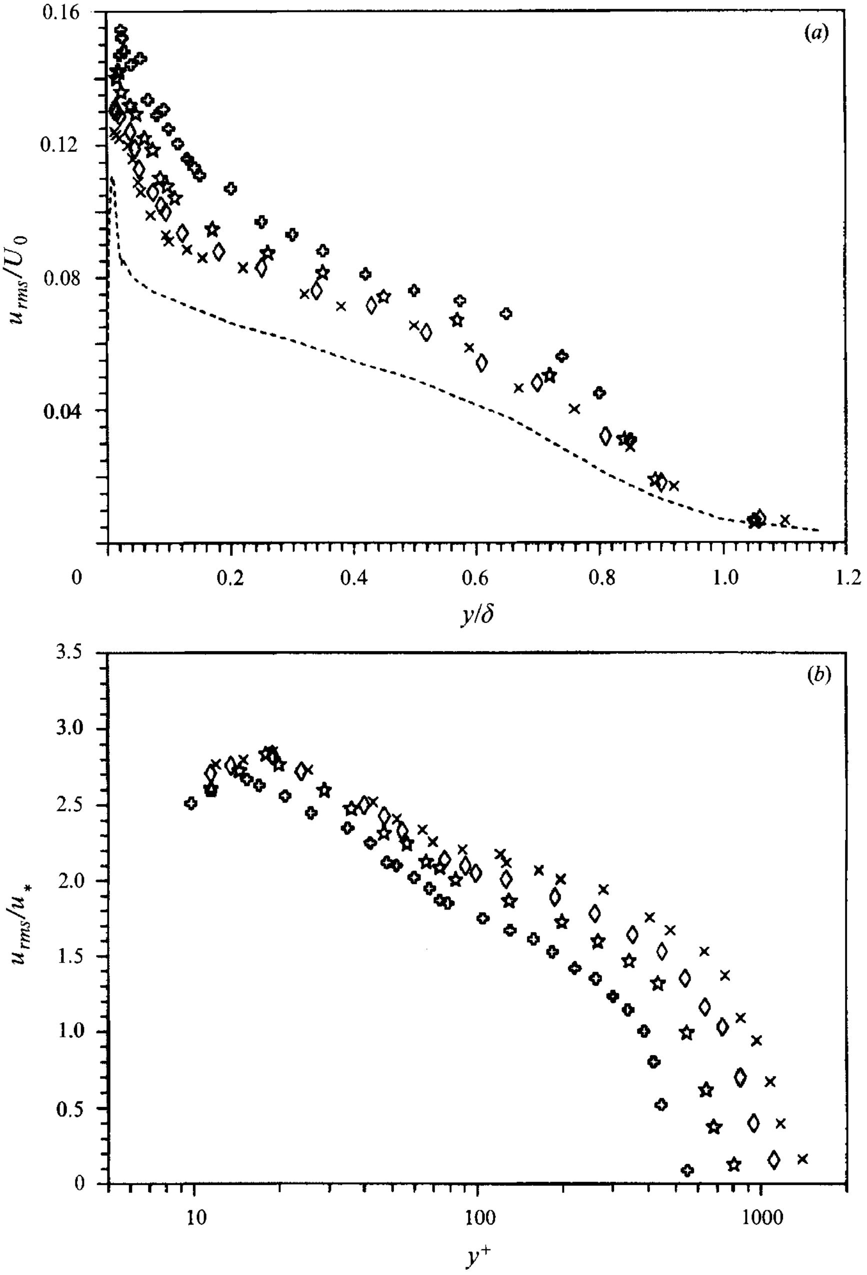

FIGURE 14. Streamwise turbulence-intensity profiles at four different Reynolds numbers. ----, Klebanoff (1963); present measurements: ×, $R_\theta = 2347$; ◇, $R_\theta = 1952$; ☆, $R_\theta = 1349$; ✣, $R_\theta = 897$.

The breakup of the log wall region,which reflects an important modulation in the structure of the turbulence (Narasimha & Sreenivasan 1979), shown in figure 16(*f*) at $R_\theta = 897$ is consistent with the observed intermittent laminarization-like phenomena discussed above in §3.1.2. The mechanism responsible for the appearance of the laminar-like flow phenomenon needs to be further studied.

Figure 17 shows that the r.m.s. values of the streamwise velocity fluctuations of the present compliant surface are lower than the corresponding rigid-surface values at

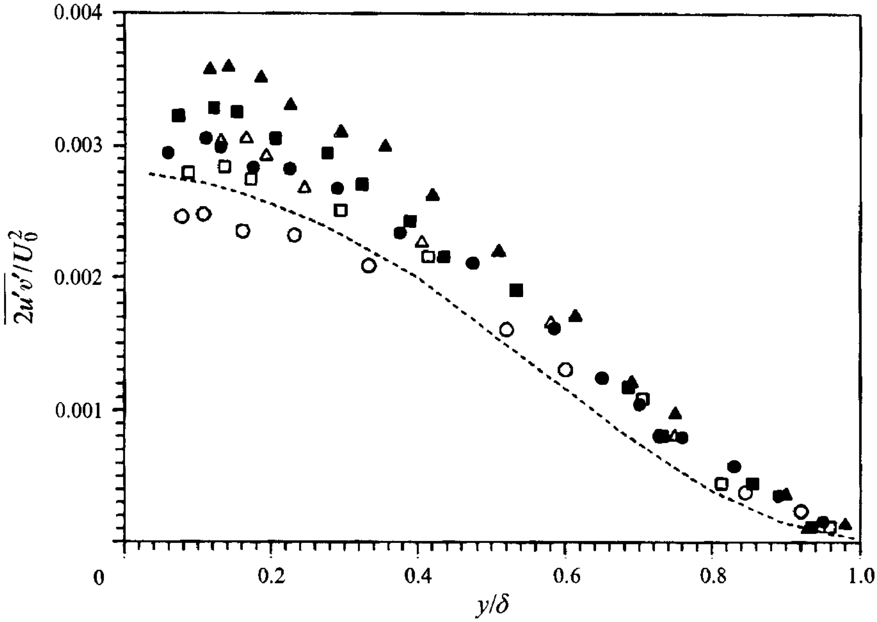

FIGURE 15. Comparisons of Reynolds-stress measurements between rigid- and compliant-surface cases at three different Reynolds number. ----, Klebanoff (1953); present measurements: rigid surface: ●, $R_\theta = 2347$; ■, $R_\theta = 1952$; ▲, $R_\theta = 1348$; compliant surface: ○, $R_\theta = 2347$; □, $R_\theta = 1952$; △, $R_\theta = 1348$.

| $R_\theta$ | $U_0$ (cm/s) | $\theta$ (mm) | $\theta/d$ | $U_0/C_t$ | $u_{*a}$ (cm/s) | $u_{*b}$ (cm/s) | $u_{*c}$ (cm/s) |
|---|---|---|---|---|---|---|---|
| | | | Rigid surface | | | | |
| 7900 | 157 | 4.43 | — | — | 5.78 | — | — |
| 5994 | 115 | 4.59 | — | — | 4.28 | — | — |
| 2752 | 51 | 4.95 | — | — | 2.07 | 2.04 | — |
| 2347 | 43 | 5.01 | — | — | 1.74 | 1.71 | 1.62 |
| 1952 | 35 | 5.11 | — | — | 1.48 | 1.43 | 1.37 |
| 1348 | 24 | 5.28 | — | — | 1.04 | 1.07 | 0.99 |
| 897 | 15 | 5.74 | — | — | 0.63 | 0.66 | — |
| | | | Compliant surface | | | | |
| 8650 | 157 | 4.49 | 0.118 | 3.32 | 5.86 | — | — |
| 6200 | 115 | 4.63 | 0.122 | 2.43 | 4.19 | — | — |
| 2850 | 51 | 4.91 | 0.129 | 1.08 | 1.95 | 1.90 | — |
| 2347 | 43 | 4.62 | 0.121 | 0.91 | 1.53 | 1.57 | 1.47 |
| 1952 | 35 | 4.78 | 0.126 | 0.74 | 1.19 | 1.24 | 1.17 |
| 1348 | 24 | 4.81 | 0.127 | 0.51 | 0.91 | 0.92 | 0.88 |
| 897 | 15 | 5.24 | 0.138 | 0.32 | — | 0.53 | — |

TABLE 2. Boundary-layer parameters. $u_{*a}$, $u_{*b}$ and $u_{*c}$ indicate friction velocities obtained by cross-plot method (*a*), wall-slope method (*b*), and Reynolds-stress measurements (*c*), separately

$R_\theta = 2347$, 1952, 1348 and 897, respectively. These measurements are consistent with the $(u^+, y^+)$ data shown in figure 16(*c*–*f*). The peak in the turbulence intensity profiles (which generally occurs at $y^+ = 12$ for a rigid-surface flat-plate turbulent boundary layer) is lowered. Also, both the buffer regions and viscous sublayers are slightly broadened or thickened. This particular compliant surface also caused a reduction in the Reynolds stress (indicated by the open symbols in figure 15) compared to the values of rigid-surface case (solid symbols). However, this reduction in $C_f$ and Reynolds stress

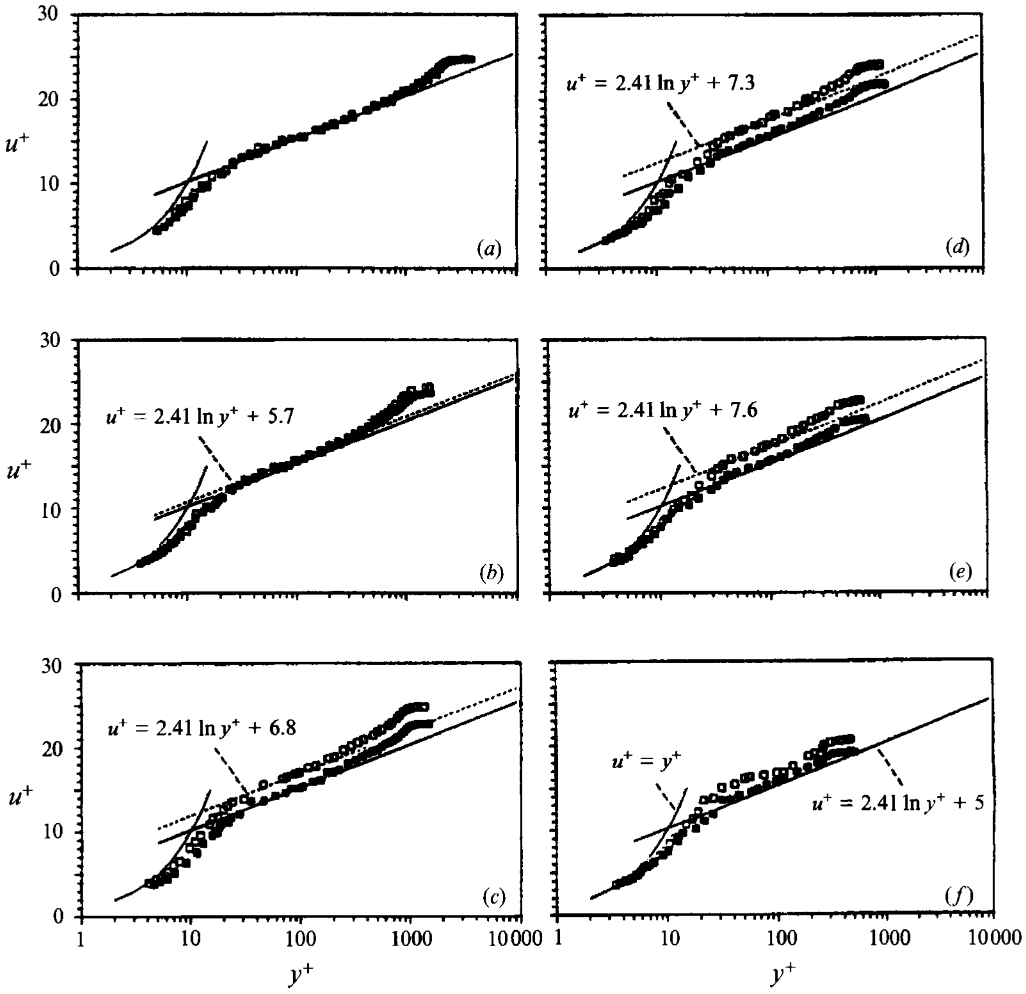

FIGURE 16. Comparisons of mean-velocity measurements between rigid- and compliant-surface cases at different Reynolds numbers. (*a*) $R_\theta = 6200$, (*b*) $R_\theta = 2850$, (*c*) $R_\theta = 2347$, (*d*) $R_\theta = 1952$, (*e*) $R_\theta = 1348$, and (*f*) $R_\theta = 897$. ----, Clauser (1956); present measurements: ■, rigid surface; □, compliant surface.

across the boundary layer occurs locally and may not result in an overall drag reduction.

## 4. Summary and conclusions

The stable boundary-layer/compliant-wall interaction (i.e. with $U_0 < R_c U_s$) of a single-layer viscoelastic compliant surface with a flat-plate turbulent boundary layer was investigated using the hydrogen-bubble flow visualization technique, in combination with holographic surface-displacement and LDA velocity-field measurements. It was found that with the presence of surface compliance there occurred: (i) an increase in $\lambda^+$ and $x_s^+$; (ii) the appearance of intermittent laminarization-like phenomenon at low $R_\theta$; (iii) a slightly broadened buffer region and viscous sublayer; (iv) an upward vertical shift in the compliant law of the wall; (v) a reduction in streamwise turbulence intensity; (vi) a local reduction in $C_f$ and Reynolds stress across the boundary layer.

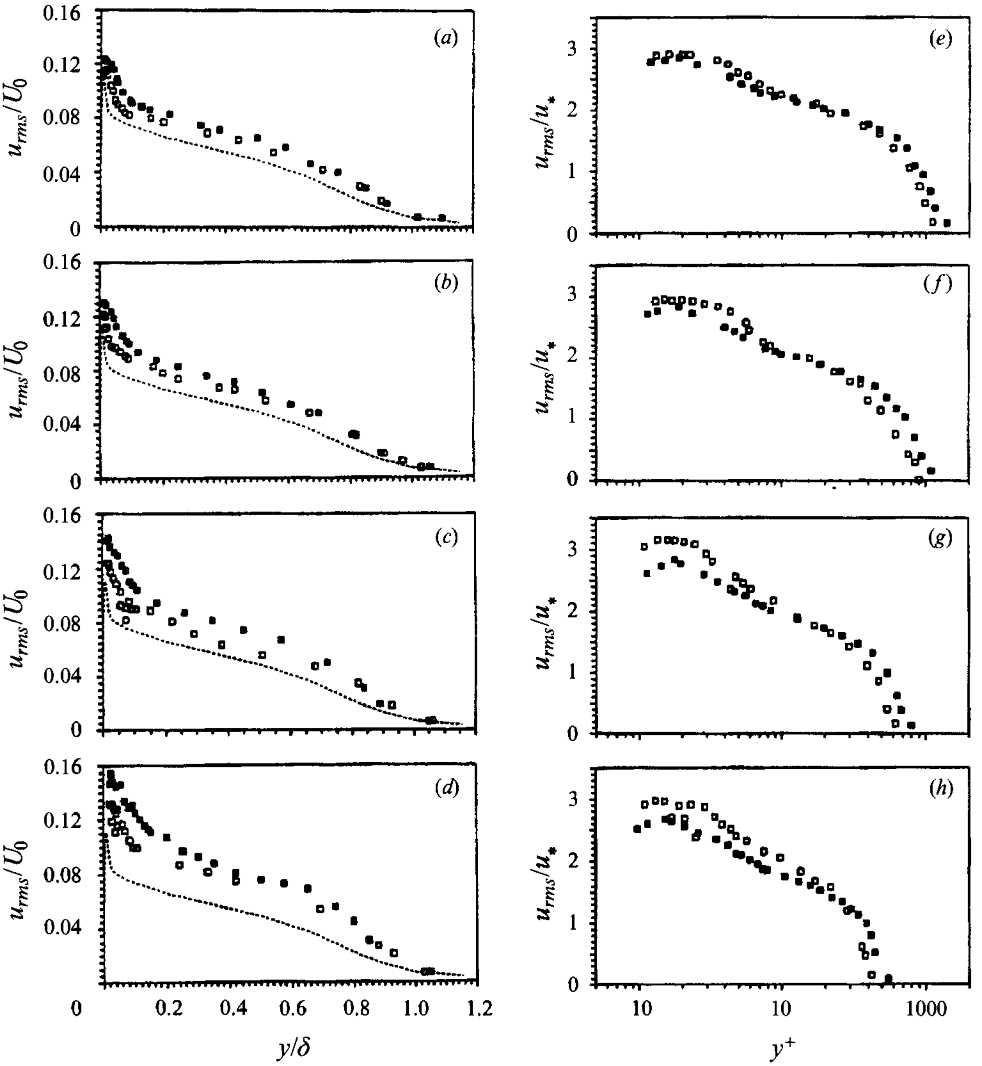

FIGURE 17. Comparisons of streamwise turbulence-intensity measurements between rigid- and compliant-surface cases at four different Reynolds numbers in both outer and inner variables. (*a*, *e*), $R_\theta = 2347$; (*b*, *f*), $R_\theta = 1952$; (*c*, *g*), $R_\theta = 1348$; (*d*, *h*), $R_\theta = 897$. ----, Klebanoff (1953); present measurements: ■, rigid surface; □, compliant surface.

In summary, visual studies associated with the mean-velocity, turbulence-intensity, and Reynolds stress measurements indicated that the surface motion modulated the flow field close to the wall; and the feedback loop which allows the turbulence to be self-sustaining seems to be broken at low Reynolds number. However, the mechanism responsible for the above observations is still not well understood. Detailed measurements of the turbulent flow field and statistical measurements of the random topography of the compliant surface are needed in order to better understand the nature of the stable fluid/compliant-surface interaction between a turbulent boundary layer and a compliant surface.

This work was supported by the Office of Naval Research under contract N00014-87-0126. Grateful acknowledgement is made to the staff of the Fluid Dynamics Group of the National Institute of Standards and Technology, especially George Mattingly, Norm Mease and David Hess without whose assistance this work would not have been accomplished.

## REFERENCES

ACHIA, B. U. & THOMPSON, D. W. 1976 Structures of the turbulent boundary in drag-reducing pipe flows. *J. Fluid Mech.* **81**, 439–464.

BLACKWELDER, R. F. & HARITONIDIS, J. H. 1979 Streamwise vortices associated with the bursting phenomenon. *J. Fluid Mech.* **94**, 577–594.

BLICK, F. B. & WALTERS, R. R. 1968 Turbulent boundary-layer characteristics of compliant surfaces. *J. Aircraft* **5**, 11–16.

BUCHHAVE, P., GEORGE, W. K. & LUMLEY, J. L. 1979 The measurement of turbulence with the laser-Doppler anemometer. *Ann. Rev. Fluid Mech.* **11**, 443–503.

BUDWIG, R. & PEATTIE, R. 1989 Two new circuits for hydrogen bubble flow visualization. *J. Phys.* E: *Sci. Instrum.* **22**, 250–254.

BUSHNELL, D. M., HEFNER, J. N. & ASH. R. L. 1977 Effect of compliant wall motion on turbulent boundary layer. *Phys. Fluids* **20**, S31-S48.

CARPENTER, P. W. 1990 Status of transition delay using compliant walls. In *Viscous Drag Reduction in Boundary Layers.* Progress in Astronautics and Aeronautics, vol. 123 (ed. Bushnell, D. M. and Hefner, J. N.), pp. 79–113. AIAA.

CARPENTER, P. W. & GARRAD, A. D. 1985 The hydrodynamic stability of flow over Kramer-type compliant surfaces. Part 1. Tollmien–Schlichting instabilities. *J. Fluid Mech.* **155**, 46.

CARPENTER, P. W. & GARRAD, A. D. 1986 The hydrodynamic stability of flow over Kramer-type compliant surfaces. Part 2. Flow-induced surface instabilities. *J. Fluid Mech.* **170**, 199.

CLAUSER, F. H. 1956 The turbulent boundary layer. *Adv. Appl. Mech.* **4**, 1–51.

COLES, D. 1962 A manual of experimental boundary-layer practice for low-speed flow. *Rand* R-304-PR, Appendix A.

CORINO, E. R. & BRODKEY, R. S. 1969 A visual study of the wall region in turbulent flow. *J. Fluid Mech.* 37, 1–37.

DONOHUE, G. L., TIEDERMAN, W. G. & REISCHMAN, M. M. 1972 Flow visualization of the near-wall region in a drag-reducing channel flow., *J. Fluid Mech.* **56**, 559–575.

DUNCAN, J. H. 1986 The response of an incompressible, viscoelastic coating to pressure fluctuations in a turbulent boundary layer. *J. Fluid Mech.* **171**, 339–363.

DUNCAN, J. H., WAXMAN, A. M. & TULIN, M. P. 1985 The dynamics of waves at the interface between a viscoelastic coating and a fluid flow. *J. Fluid Mech.* **158**, 177–197.

ERM, L. P. & JOUBERT, P. N. 1991 Low-Reynolds-number turbulent boundary layers. *J. Fluid Mech.* **230**, 1–44.

GAD-EL-HAK, M. 1986*a* Boundary layer interactions with a compliant coating: An overview. *Appl. Mech. Rev.* **39**, 511–523.

GAD-EL-HAK, M. 1986*b* The response of elastic and viscoelastic surfaces to a turbulent boundary layer. *Trans. ASME* E: *J. Appl. Mech.* **53**, 206–212.

GAD-EL-HAK, M. 1987 Compliant coatings research: A guide to the experimentalist. *J. Fluids Struct.* **1**, 55–70.

GAD-EL-HAK, M., BLACKWELDER, R. F & RILEY, J. J. 1984 On the interaction of compliant coatings with boundary-layer flows. *J. Fluid Mech.* **140**, 257–280.

GRANVILLE, P. S. 1977 Drag and turbulent boundary layer of flat plates at low Reynolds numbers. *J. Ship Res.* **21**, 1.

GRASS, A. J. 1971 Structural features of turbulent flow over smooth and rough boundaries. *J. Fluid Mech.* **50**, 233–255.

GUPTA, A. K., LAUFER, J. & KAPLAN, R. E. 1971 Spatial structure in the viscous sublayer. *J. Fluid Mech.* **50**, 493–512.

HANSEN, R. J. & HUNSTON, D. L. 1974 An experimental study of turbulent flows over compliant surfaces. *J. Sound Vib.* **34**, 297–308.

HANSEN, R. J. & HUNSTON, D. L. 1983 Fluid-property effects on flow-generated waves on a compliant surface. *J. Fluid Mech.* **133**, 161–177.

HANSEN, R. J., HUNSTON, D. L. & NI, C. C. 1980 An experimental study of flow-generated waves on a flexible surface. *J. Sound Vib.* **68**, 317–334.

HESS, D. E. 1990 An experimental investigation of a compliant surface beneath a turbulent boundary layer. PhD dissertation, The Johns Hopkins University.

HESS, D. E., PEATTIE, R. A. & SCHWARZ, W. H. 1993 A non-invasive method for the measurement of flow-induced surface displacement of a compliant surface. *Exp. Fluids* **14**, 78–84.

JOHNSON, P. L. & BARLOW, R. S. 1989 Effect of measuring volume length on two-component laser velocimeter measurements in a turbulent boundary layer. *Exp. Fluids* **8**, 137–144.

KIM, H. T., KLINE, S. J. & REYNOLDS, W. C. 1971 The production of turbulence near a smooth wall in a turbulent boundary layer. *J. Fluid Mech.* **50**, 133–160.

KLEBANOFF, P. S. 1953 Characteristics of turbulence in a boundary layer with zero pressure gradient. *NBS Rep.* 2454.

KLINE, S. J., REYNOLDS, W. C., SCHRAUB, F. A. & RUNDSTADLER, P. W. 1967 The structure of turbulent boundary layer. *J. Fluid Mech.* **30**, 741–773.

KRAMER, M. O. 1957 Boundary layer stabilization by distribution damping. *J. Aero. Sci.* **41**, 259–281.

LEE, M. K., ECKELMANN, L. D. & HANRATTY, T. J. 1974 Identification of turbulent wall eddies through the phase relation of the components of the fluctuating velocity gradient. *J. Fluid Mech.* **66**, 17–33.

LEE, T., FISHER, M. & SCHWARZ, W. H. 1993 The measurement of flow-induced surface displacement on a compliant surface by optical holographic interferometry. *Exp. Fluids* **14**, 159–168.

LU, L. J. & SMITH, C. R. 1991 Use of flow visualization data to examine spatial-temporal velocity and burst-type characteristic in a turbulent boundary layer. *J. Fluid Mech.* **232**, 303–340.

MCMICHAEL, J. M., KLEBANOFF, P. S. & MEASE, N. 1979 Experimental investigation of drag on a compliant surface. In *Viscous Flow Drag Reduction* (ed. G. R. Hough), *AIAA Astro. Aero.*, vol. 72, pp. 410–438.

MURLIS, J., TSAI, H. M. & BRADSHAW, P. 1982 The structure of turbulent boundary layers at low Reynolds numbers. *J. Fluid Mech.* **122**, 13–56.

NAKAGAWA, H. & NEZU, I. 1981 Structure of space-time correlations of bursting phenomena in a open-channel flow. *J. Fluid Mech.* **104**, 1–43.

NARASIMHA, R. & SREENIVASAN, K. R. 1979 Relaminarization of fluid flows. *Adv. Appl. Mech.* **19**, 221–309.

OLDAKER, D. K. & TIEDERMAN, W. G. 1977 Spatial structure of the viscous sublayer in drag-reducing channel flows. *Phys. Fluids* **220**, S133.

PRESTON, J. H. 1958 The minimum Reynolds number for a turbulent boundary layer and the selection of transition device. *J. Fluid Mech.* **3**, 373–384.

PURTELL, L. P., KLEBANOFF, P. S. & BUCKLEY, F. T. 1981 Turbulent boundary layer at low Reynolds number *Phys. Fluids* **24**, 802–811.

RILEY, J. J., GAD-EL-HAK, M. & METCALF, R. W. 1988 Compliant coatings. *Ann. Rev. Fluid Mech.* **20**, 393–420.

SCHRAUB, F. A., KLINE, S. J., HENRY, J., RUNSTADLER, P. W. & LITTELL, A. 1965 Use of hydrogen bubbles for quantitative determination of time-dependent velocity fields in low-speed water flows. *Trans. ASME* D: *J. Basic Engng, June*, 429–444.

SMITH, C. R. & METZLER, S. P. 1983 The characteristics of low-speed streaks in the near-wall region of a turbulent boundary layer. *J. Fluid Mech.* **129**, 27–54.

SMITS, A. J., MATHESON, N. & JOUBERT, P. N. 1983 Low-Reynolds-number turbulent boundary layers in zero and favourable pressure gradient. *J. Ship Res.* **27**, 147.

TIEDERMAN, W. G., LUCHIK, T. S. & BOGARD, D. G. 1985 Wall-layer structure and drag reduction. *J. Fluid Mech.* **156**, 419–437.

WALKER, D. T. & TIEDERMAN, W. G. 1990 Turbulent structure in a channel flow with polymer injection at the wall. *J. Fluid Mech.* **218**, 377–403.

WEI, T. & WILLMARTH, W. W. 1989 Reynolds-number effects on the structure of a turbulent channel flow. *J. Fluid Mech.* **204**, 57–95.

YEO, K. S. 1988 The stability of boundary-layer flow over single- and multi-layer viscoelastic walls. *J. Fluid Mech.* **196**, 359.